JGP Journal of General Physiology

ARTICLE

Reduced voltage-activated Ca^{2+} release flux in muscle fibers from a rat model of Duchenne dystrophy

Jonathan Schreiber[1], Ludivine Rotard[1], Yves Tourneur[2], Aude Lafoux[3], Christine Berthier[1], Bruno Allard[1], Corinne Huchet[3,4], and Vincent Jacquemond[1]

The potential pathogenic role of disturbed Ca^{2+} homeostasis in Duchenne muscular dystrophy (DMD) remains a complex, unsettled issue. We used muscle fibers isolated from 3-mo-old *DMD*^{mdx} rats to further investigate the case. Most *DMD*^{mdx} fibers exhibited no sign of trophic or morphology distinction as compared with WT fibers and mitochondria and t-tubule membrane networks also showed no stringent discrepancy. Under voltage clamp, values for holding current were similar in the two groups, whereas values for capacitance were larger in *DMD*^{mdx} fibers, suggestive of enhanced amount of t-tubule membrane. The Ca^{2+} current density across the channel carried by the EC coupling voltage sensor ($Ca_V1.1$) was unchanged. The maximum rate of voltage-activated sarcoplasmic reticulum (SR) Ca^{2+} release was reduced by 25% in the *DMD*^{mdx} fibers, with no change in voltage dependency. Imaging resting Ca^{2+} revealed rare spontaneous local SR Ca^{2+} release events with no sign of elevated activity in *DMD*^{mdx} fibers. Under current clamp, *DMD*^{mdx} fibers generated similar trains of action potentials as WT fibers. Results suggest that reduced peak amplitude of SR Ca^{2+} release is an inherent feature of this DMD model, likely contributing to muscle weakness. This occurs despite a preserved amount of releasable Ca^{2+} and with no change in excitability, $Ca_V1.1$ channel activity, and SR Ca^{2+} release at rest. Although we cannot exclude that fibers from the 3-mo-old animals do not yet display a fully developed disease phenotype, results provide limited support for pathomechanistic concepts frequently associated with DMD such as membrane fragility, excessive Ca^{2+} entry, or enhanced SR Ca^{2+} leak.

Introduction

A number of mechanisms involved in the control of Ca^{2+} homeostasis and excitation–contraction (EC) coupling have been reported altered in dystrophin-deficient muscle cells. This is now to the point that emphasizing abnormal or defective Ca^{2+} homeostasis in the associated Duchenne muscular dystrophy (DMD) disease situation has become a common place, with cytosolic Ca^{2+} overload being one frequently assumed pathogenic driver of multiple detrimental effects. Specifically, altered Ca^{2+} fluxes at the plasma/t-tubule membrane level have been reported to be carried by (1) membrane tearing (Mokri and Engel, 1975; Pestronk et al., 1982; Petrof et al., 1993; Pasternak et al., 1995), (2) TRPC or other types of sarcolemmal Ca^{2+} leak channels (Fong et al., 1990; Franco and Lansman, 1990; Mallouk and Allard, 2002; Vandebrouck et al., 2002; Ducret et al., 2006; Gervásio et al., 2008; Krüger et al., 2008; Teichmann et al., 2008; Millay et al., 2009; Matsumura et al., 2011; Lin et al., 2022), (3) the store-operated Ca^{2+} entry complex (Boittin et al., 2006; Edwards et al., 2010; Cully et al., 2012; Zhao et al., 2012; García-Castañeda et al., 2022), (4) connexin hemichannels (Cea et al., 2016; Nouet et al., 2020), and (5) P2X purinoreceptors (Jiang et al., 2005; Yeung et al., 2006); in intracellular compartments by sarcoplasmic reticulum (SR) ryanodine receptors (Woods et al., 2004; Hollingworth et al., 2008; Bellinger et al., 2009; Cully and Launikonis, 2016; Cully and Rodney, 2020), inositol 1,4,5-trisphosphate receptors (Balghi et al., 2006a, 2006b; Mondin et al., 2009; Cárdenas et al., 2010), and the SERCA pump (Divet and Huchet-Cadiou, 2002; Morine et al., 2010; Schneider et al., 2013; Kargacin and Kargacin, 2016); and there are also reported changes in the expression level of Ca^{2+}-binding proteins (Niebroj-Dobosz et al., 1989a, 1989b; Doran et al., 2004; Lohan and Ohlendieck, 2004; Balghi et al., 2006b; Pertille et al., 2010). Still, in most cases, there remains considerable uncertainty as to up to what extent these changes affect physiological Ca^{2+} cycling in intact muscle fibers and whether or not they play a significant role in either muscle fiber weakness or muscle fiber necrosis. Detection of membrane current and

[1]University Lyon, Université Claude Bernard Lyon 1, CNRS UMR-5261, INSERM U-1315, Institut NeuroMyoGène - Pathophysiology and Genetics of Neuron and Muscle, Lyon, France; [2]UFPE Department Nutrição, Cidade Universitária, Recife, Brazil; [3]Therassay Platform, CAPACITES, Nantes Université, Nantes, France; [4]Nantes Gene Therapy Laboratory, Nantes Université, INSERM UMR TARGET 1089, Nantes, France.

Correspondence to Vincent Jacquemond: vincent.jacquemond@univ-lyon1.fr.

cytosolic Ca^{2+} under voltage control in intact isolated muscle fibers offers exclusive integrative insights into the plasma membrane integrity, ion channel activity, and intracellular Ca^{2+} regulation with specific relevance to EC coupling function. We have used this approach, complemented by confocal imaging of associated relevant parameters, in muscle fibers isolated from DMD^{mdx} rats (Larcher et al., 2014). The rationale is that most previous studies relied on the C57BL/10ScSn *mdx* (from here on referred to as *mdx*) mouse model of DMD, which is commonly admitted to exhibit a mild, nonprogressive disease phenotype (see for review Willmann et al., 2009; McGreevy et al., 2015; Wilson et al., 2017). In comparison, the DMD^{mdx} rat exhibits a progressively aggravating status characterized, between 3 and 7 mo of age, by a loss of body weight and of muscle mass and myonecrosis/-degeneration (Larcher et al., 2014). DMD^{mdx} rat muscles also present with fibrosis that expands with time, resulting in marked endomysial and perimysial infiltration of connective tissue in 7-mo-old animals (Larcher et al., 2014). In contrast, fibrosis remains minimal in muscles other than the diaphragm in the *mdx* mouse (Tanabe et al., 1986; Stedman et al., 1991). DMD^{mdx} rats suffer from defects in cardiac structure and function in 3-mo-old animals, which become more severe with time (Larcher et al., 2014), with the extent of cardiac fibrous area being doubled between 3 and 7 mo of age. In *mdx* mice, although MRI is able to identify early cardiac abnormalities, cardiac defects are usually reported less pronounced and/or to develop over a more delayed time frame (Quinlan et al., 2004; Van Erp et al., 2010; Stuckey et al., 2012). At last, the *mdx* mouse exhibits a slightly reduced lifespan relative to WT mice (Pastoret and Sebille, 1995; Chamberlain et al., 2007), whereas median survival of the DMD^{mdx} rat is ∼1 year (Huchet, C., personal communication). Of importance, the severity of the DMD disease in the rat has been confirmed in the other DMD rat models developed by Nakamura et al. (2014) and Taglietti et al. (2022), which also showed progressive and severe skeletal muscle loss associated with fibrotic deposition and fat infiltration leading to severe muscle, respiratory, and cardiac dysfunction, resulting in premature death (at ∼1 year of age, Taglietti et al., 2022). Altogether, there are thus clear indications that the DMD^{mdx} rat reproduces classical features of Duchenne dystrophy patients better than the *mdx* mouse. We speculated that it could help enlighten the DMD Ca^{2+} issue.

Materials and methods

This work was achieved following the ethics principles of the French Department of Veterinary Services and the French Ministry for Higher Education, Research and Innovation, in accordance with the guidelines of the local committee in charge of animal well-being (SBEA) at the University of Nantes, the French Ministry of Agriculture (decree 87/848), and the revised European Directive 2010/63/EU. Animals were housed at the accredited Therassay (University of Nantes) animal facility. Investigations were approved by the Ethics Committee on Animal Experimentation of the Pays de la Loire Region, in accordance with the guidelines from the French National Research Council for the Care and Use of Laboratory Animals (APAFIS#10792–2017061316021120).

Isolation and preparation of muscle fibers for electrophysiology

Experiments were performed on muscle fibers isolated from the flexor digitorum brevis (FDB) muscles of 3-mo-old WT and DMD^{mdx} littermate male rats (Larcher et al., 2014). Rats were sacrificed by intravenous administration of sodium pentobarbital (300 mg, Dolethal; Vetoquinol UK Ltd.). All procedures for fiber isolation and preparation for silicone-clamp electrophysiology were identical to those described in our previous works (e.g., Sanchez et al., 2021; Jaque-Fernandez et al., 2023). In brief, FDB muscles were dissected and stored at 4°C in Tyrode solution during 6 h, the time needed for dedicated express transport from Nantes to Lyon. Muscles were then incubated for 60 min at 37°C in Tyrode solution containing 2 mg/ml collagenase (Sigma-Aldrich type 1). Single isolated fibers were obtained by gentle mechanical trituration of the muscles within the experimental chamber (50-mm-wide culture µ-dish; Ibidi). For this, the µ-dish had its floor covered with a thin layer of silicone grease and was then filled with culture medium containing 10% bovine fetal serum (MI199; Eurobio). Following mechanical trituration of an FDB muscle, single isolated fibers were partially covered with silicone so that an end portion of fiber ∼100–200 µm long remained silicone free, in contact with the extracellular medium. For voltage clamp experiments, the culture medium was then replaced by our standard TEA-containing extracellular solution. The tip of a borosilicate glass micropipette filled with a solution mimicking the composition of the intracellular medium (intracellular-like solution, see Solutions section) and also containing the Ca^{2+}-sensitive dye rhod-2 and 15 mM EGTA was inserted in the silicone-embedded portion of fiber. The chloride silver wire in the micropipette was connected to an RK400 amplifier (Bio-Logic). A 30-min period of equilibration was allowed before delivering voltage clamp pulses from a holding voltage of −80 mV. For action potential (AP) measurements, the culture medium was replaced by Tyrode solution and the micropipette was filled with the intracellular-like solution. Following impalement of the silicone-embedded portion of fiber, the current-clamp mode of the amplifier was established and a 5-min period of equilibration was allowed before delivering short (typically 0.5-ms-long) suprathreshold depolarizing current pulses to trigger APs at frequencies ranging between 1 and 80 Hz over a 3-s duration. The resting membrane potential was maintained at −80 mV by passing a constant hyperpolarizing current. All experiments were performed at room temperature (20–22°C).

$Ca_V1.1$ Ca^{2+} current

Voltage-clamped fibers were depolarized by 0.5-s-long depolarizing test pulses from −50 to +60 mV. The linear component of the current was removed by subtracting the appropriately scaled value of the steady current measured at the end of a 0.5-s-long −20 mV step applied before each test pulse. This did not entirely eliminate the outward current measured during pulses to values between −50 and −30 mV, below the activation threshold of the Ca^{2+} current. For this reason, the voltage dependence of peak Ca^{2+} current (values normalized to the capacitance) was fitted with the following equation which included a linear slope component:

$$I(V) = G_{max}(V - V_{rev})/\{1 + [\exp(V_{0.5} - V)/k]\} + slope(V + 80),$$

with $I(V)$ the peak current density at the command voltage V, G_{max} the maximum conductance, V_{rev} the apparent reversal potential, $V_{0.5}$ the half-activation potential, k the steepness factor, and *slope* the conductance of the residual linear component.

Ca^{2+} imaging and Ca^{2+} release calculation

Procedures were similar to those described previously for mouse muscle fibers (e.g., Kutchukian et al., 2016; Jaque-Fernandez et al., 2020). A Zeiss LSM 800 microscope equipped with a 63× oil immersion objective (numerical aperture 1.4) was used. Measurements of voltage clamp–activated rhod-2 Ca^{2+} transients were achieved with the line-scan (x,t) mode of the microscope: a 50.7-µm-long line was scanned every 1.02 ms using excitation from the 561-nm diode laser. Rhod-2 fluorescence transients were expressed as F/F_0, F_0 being the pre-pulse baseline fluorescence. Quantification of the Ca^{2+} release flux (dCa_{Tot}/dt) from the rhod-2 fluorescence transients was achieved according to previously described procedures (e.g., Kutchukian et al., 2016). In brief, the time derivative of the total released Ca^{2+} ($[Ca_{Tot}]$) was calculated from the occupancy of intracellular Ca^{2+}-binding sites and Ca^{2+} transported back across the SR membrane by the SERCA pump. For this, changes in (Ca^{2+}) were calculated from the rhod-2 transients using the pseudo-ratio equation described by Cheng et al. (1993), assuming a resting $[Ca^{2+}]$ level of 0.1 µM and an equilibrium dissociation constant of 1.2 µM. From this, the time course of Ca^{2+} bound to troponin C, to parvalbumin, and of Ca^{2+} back-transported across the SR membrane by the SERCA pump were calculated using values described by Sanchez et al. (2021) for binding sites concentrations, equilibrium dissociation constants, and *on* and *off* rate constants, and with the value for maximum pump rate assumed to be 5 $\mu M.ms^{-1}$. This value was adapted from the 3.14–4.49 $\mu M.ms^{-1}$ range estimated by Garcia and Schneider (1993) in rat fast-twitch fibers, taking into account the difference in temperature (16°C versus 20–22°C in our conditions). For Ca^{2+} binding to EGTA, the total concentration of effective binding sites was assumed to be 7.2 mM, and values for *on* and *off* rate constants and corresponding equilibrium dissociation constant were taken from the Ca^{2+}-removal analysis performed by Schuhmeier and Melzer (2004): 0.02 $\mu M^{-1}.ms^{-1}$, 0.00271 ms^{-1}, and 0.1355 µM, respectively. With the large concentration of EGTA used in our experiments, Ca-EGTA makes a predominant contribution to the calculated Ca^{2+} release flux.

The voltage dependence of the peak Ca^{2+} release flux from each muscle fiber was fitted with a Boltzmann function:

$$dCa_{Tot}/dt = Max\, dCa_{Tot}/dt/\{1 + \exp[(V_{0.5} - V)/k]\},$$

with $Max\ dCa_{Tot}/dt$ the maximum Ca^{2+} release flux, $V_{0.5}$ the mid-activation voltage, and k the steepness factor.

Imaging of t-tubule and mitochondria networks

This was achieved with the 63× oil immersion objective of the same above-mentioned Zeiss LSM 800 microscope. For t-tubule staining, single isolated FDB muscle fibers dispersed within an Ibidi µ-dish filled with Tyrode solution were incubated for 60 min in the presence of 10 µM of Di-8-anepps. For mitochondria staining, separate batches of fibers were incubated under the same conditions in the presence of 10 nM tetramethyl rhodamine methyl ester (TMRM) for 10 min. Di-8-anepps and TMRM fluorescence were imaged using excitation from the 488 and 561-nm diode lasers, respectively. Quantification was achieved with ImageJ (National Institutes of Health) from frames of 512 × 512 pixels at 0.2 and 0.1 µm per pixel for Di-8-anepps and TMRM and Di-8-anepps, respectively.

The t-tubule density was estimated following the approach described by Kutchukian et al. (2017). The largest possible region of interest excluding the plasma membrane was selected. Automatic Otsu's method thresholding was used to create a binary image of the surface area occupied by t-tubules. A t-tubule density index was calculated as the percentage of positive pixels within the region. Analysis was performed within two images taken at distinct locations of each fiber, and the two corresponding index values were averaged. The coefficient of variation for the t-tubule density index was 10.2% and 7.9% in the WT and DMD^{mdx} groups, respectively. Of note, different from the initial procedure described by Kutchukian et al. (2017), the "skeletonize" function was not used to delineate the t-tubule network (as also done in Ghasemizadeh et al. [2021]). For measurements of the distance between adjacent t-tubules, average fluorescence profiles were generated from a large region of interest (e.g., Kutchukian et al., 2017) in two images taken at distinct locations of each fiber. The average peak-to-peak distance was measured from each profile and the mean from the two images was calculated. Under the conditions used, lateral resolution is ∼200 nm. The coefficient of variation for t-tubule spacing was 2.9% and 3.1% in WT and DMD^{mdx} groups, respectively.

From the TMRM images, ImageJ isodata method thresholding followed by particle analysis was used to compare the area of what is referred to as mitochondrial objects, between the two groups.

Imaging of spontaneous Ca^{2+} release events

Single isolated FDB muscle fibers dispersed within an Ibidi µ-dish filled with Tyrode solution were incubated for 30 min in the presence of 10 µM Fluo-4 acetoxymethyl ester. Recording and quantification of Ca^{2+} release events were achieved similarly to previously described procedures (see Jaque-Fernandez et al., 2020). In brief, two series of 40 consecutive confocal frames of Fluo-4 fluorescence (512 × 512 pixels at 0.2 µm per pixel, 636 ms per frame) were acquired in each fiber. Images in each stack were smoothed and the SD of fluorescence intensity at each pixel position, along the stack, was calculated. The 20% largest values in the SD image were removed to calculate the mean SD of silent areas. Active areas were then defined as pixel positions exhibiting at least 1.5× larger values of SD than the mean SD value from silent areas.

Solutions

Tyrode solution contained (in mM) 140 NaCl, 5 KCl, 2.5 $CaCl_2$, 2 $MgCl_2$, and 10 HEPES. The standard extracellular solution for voltage clamp experiments contained (in mM): 140 TEA-methane-sulfonate, 2.5 $CaCl_2$, 2 $MgCl_2$, 1 4-aminopyridine, 10 HEPES,

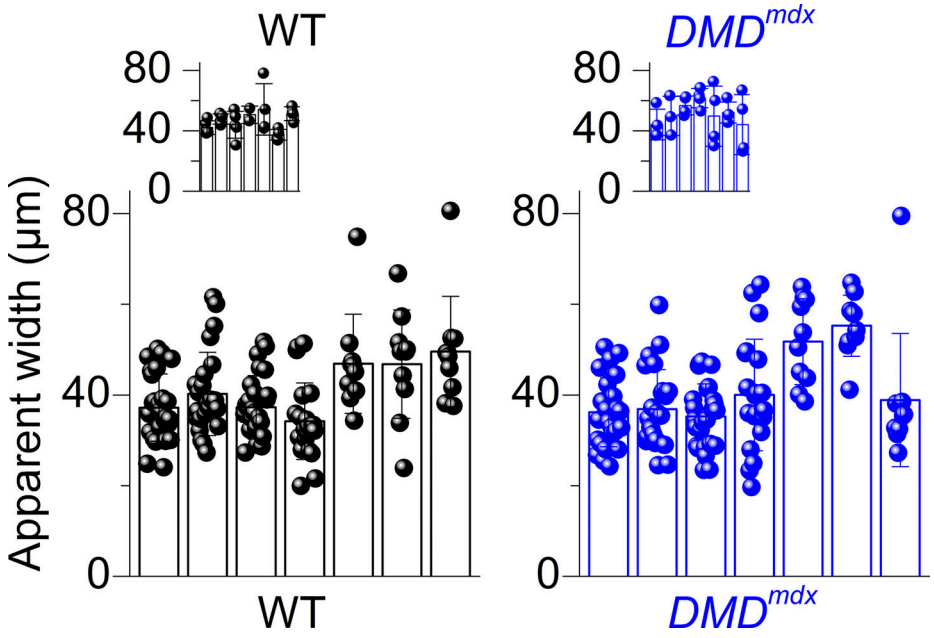

Figure 1. **Apparent width of WT and *DMD*^{mdx} muscle fibers.** Individual and corresponding mean (±SD) values for the apparent width of WT and *DMD*^{mdx} fibers (n = 126 fibers from seven animals in each group). Five measurements were taken from each fiber, using equally spaced lines, transverse to the longitudinal axis. Each data point corresponds to the average from these five measurements. Each bar (and superimposed data points) shows data from a same animal. Main graphs show values from fibers used for di-8-anepps, TMRM, and Fluo-4 staining. WT and *DMD*^{mdx} values did not significantly differ (P = 0.95, nested t test, 95% CI for the difference between mean values: −7.8 to 8.3). Insets shows values from the voltage-clamped fibers (n = 29 fibers from seven WT animals and 27 fibers from seven *DMD*^{mdx} animals. P = 0.17, nested t test, 95% CI for the difference between mean values: −2.4 to 12.0). 95% CI, 95% confidence interval.

and 0.002 tetrodotoxin. The standard intracellular-like solution contained (in mM): 120 K-glutamate, 5 Na_2-ATP, 5 Na_2-phosphocreatine, 5.5 $MgCl_2$, 5 glucose, and 5 HEPES. For measurements of rhod-2 Ca^{2+} transients, it also contained 15 EGTA, 6 $CaCl_2$, and 0.1 rhod-2. All solutions were adjusted to pH 7.20.

Data and statistical analysis

Randomization was not used, and experimenters were not blinded to the source of the muscle fibers being studied. Individual data points and corresponding mean ± SD values are presented for groups of fibers from a same animal. Statistical comparison was achieved using a hierarchical/nested analysis implemented in GraphPad Prism 10 software (Eisner, 2021) preventing pseudoreplication: measurements from fibers from the same animal were considered as technical replicates; clustering of replicates from the same animal was corrected for by the hierarchical approach (see Sikkel et al., 2017). Unless otherwise stated, this procedure was used for comparison of all parameters between the WT and *DMD*^{mdx} groups. For negative results (P > 0.05), the 95% confidence interval for the difference between the mean value in the *DMD*^{mdx} group minus the mean value in the WT group is given. In all presented bar graphs, each individual bar represents one animal and each symbol represents a fiber from that animal.

Results

T-tubule and mitochondria networks in *DMD*^{mdx} muscle fibers

Enzymatic dissociation of the FDB muscles generated generous batches of healthy-looking muscle fibers, the WT and *DMD*^{mdx} groups being qualitatively indistinguishable, except from the routine presence of 10–15% branched *DMD*^{mdx} fibers. Those were not included in any of the present analysis. No difference in apparent fiber width could be detected between the WT and *DMD*^{mdx} groups (Fig. 1). Staining of the plasma membrane/t-tubules with Di-8-anepps revealed a globally unaltered network (Fig. 2 A) in *DMD*^{mdx} fibers, with no sign of change in t-tubule density nor in t-tubule transverse spacing (Fig. 2 B). Dystrophin-deficient muscles were reported to suffer from a decline in mitochondria function and content (see Reid and Alexander, 2021), although not all studies concur on this issue, possibly because of the heterogeneous nature of mitochondrial stress during progression of the disease (Bellissimo et al., 2022). We took advantage of our isolated fiber preparation to examine the mitochondrial network pattern using TMRM staining (Desai et al., 2023).

The red images in Fig. 3 A correspond to the TMRM fluorescence from the above shown transmitted light images of a WT and a *DMD*^{mdx} muscle fiber. Overall, there was no striking difference that could be visually pinpointed between the two groups of images. The density of staining, normalized to fiber surface area, did not differ between the two groups (P = 0.16, nested t test, 95% confidence interval for the difference between mean values: −2.8 to 13.9), with mean (±SD) values from the four WT animals being 20.2 ± 2.5% (n = 5 fibers), 20.7 ± 3.9% (n = 6 fibers), 27.1 ± 4.6 (n = 5 fibers), and 20.3 ± 5.2% (n = 10 fibers), and mean values from the four *DMD*^{mdx} animals being 28.3 ± 4.5% (n = 5 fibers), 27.6 ± 8.1% (n = 6 fibers), 34.5 ± 9.3% (n = 5 fibers), and 20.7 ± 5.8% (n = 10 fibers).

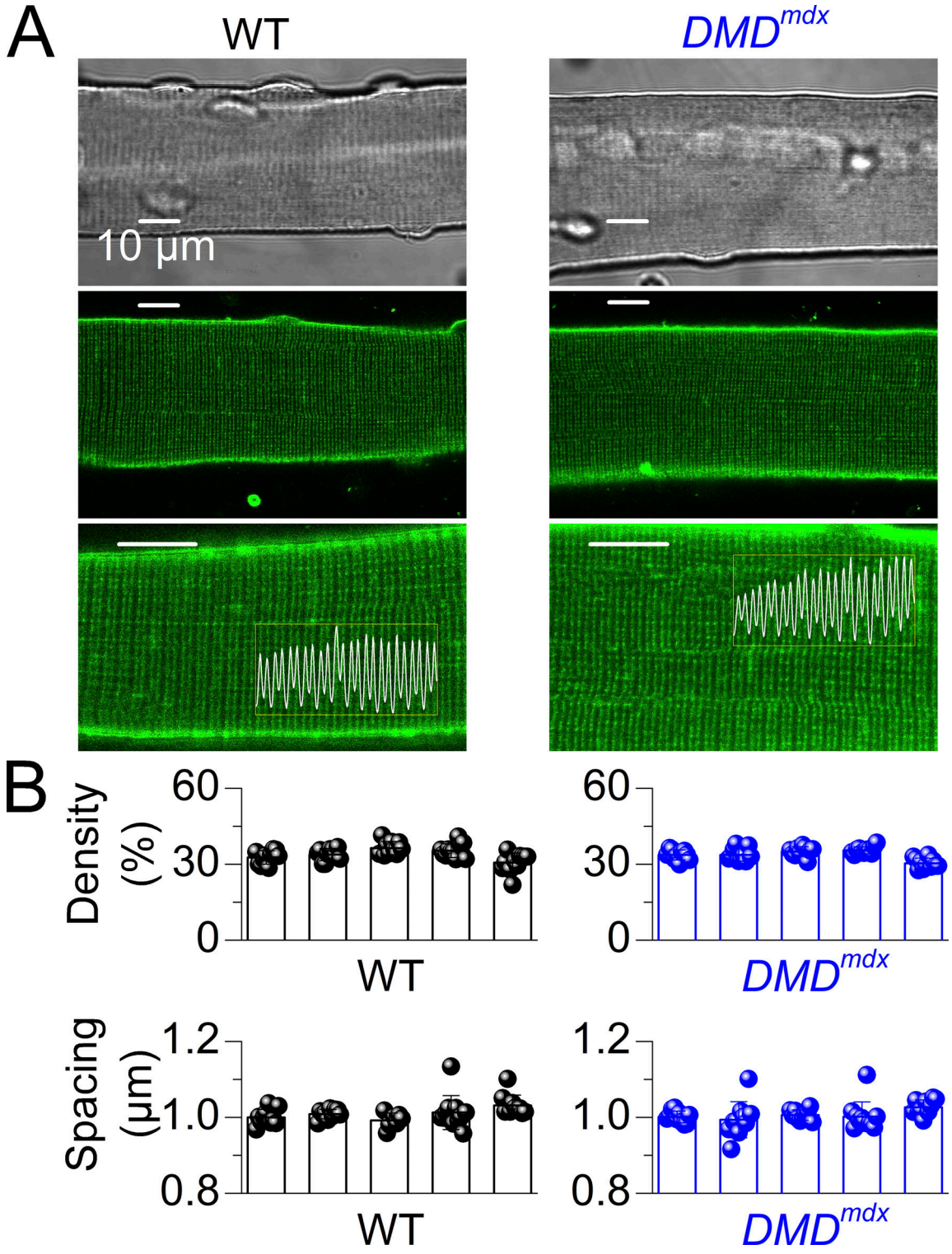

Figure 2. **T-tubule network in WT and *DMD*^{mdx} muscle fibers. (A)** Confocal images of di-8-anepps fluorescence in a WT and in a *DMD*^{mdx} fiber, at two magnifications. The white trace superimposed on each bottom image corresponds to the average fluorescence intensity profile along the region of interest enclosed within the yellow rectangle. Transmitted light images are shown on top. All scale bars correspond to 10 µm. **(B)** Top: Individual and corresponding mean (±SD) values for the t-tubule density index in WT and *DMD*^{mdx} fibers (n = 52 fibers from five animals in each group. P = 0.94, nested t test, 95% CI for the difference between mean values: −3.2 to 3.0). Bottom: Individual and corresponding mean (±SD) values for the average distance between adjacent t-tubules (spacing) in WT and *DMD*^{mdx} fibers (n = 48 fibers from five WT animals and n = 51 fibers from five *DMD*^{mdx} animals. P = 0.61, nested t test, 95% CI for the difference between mean values: −0.023 to 0.015). Each bar and superimposed data points correspond to data from a same animal. 95% CI, 95% confidence interval.

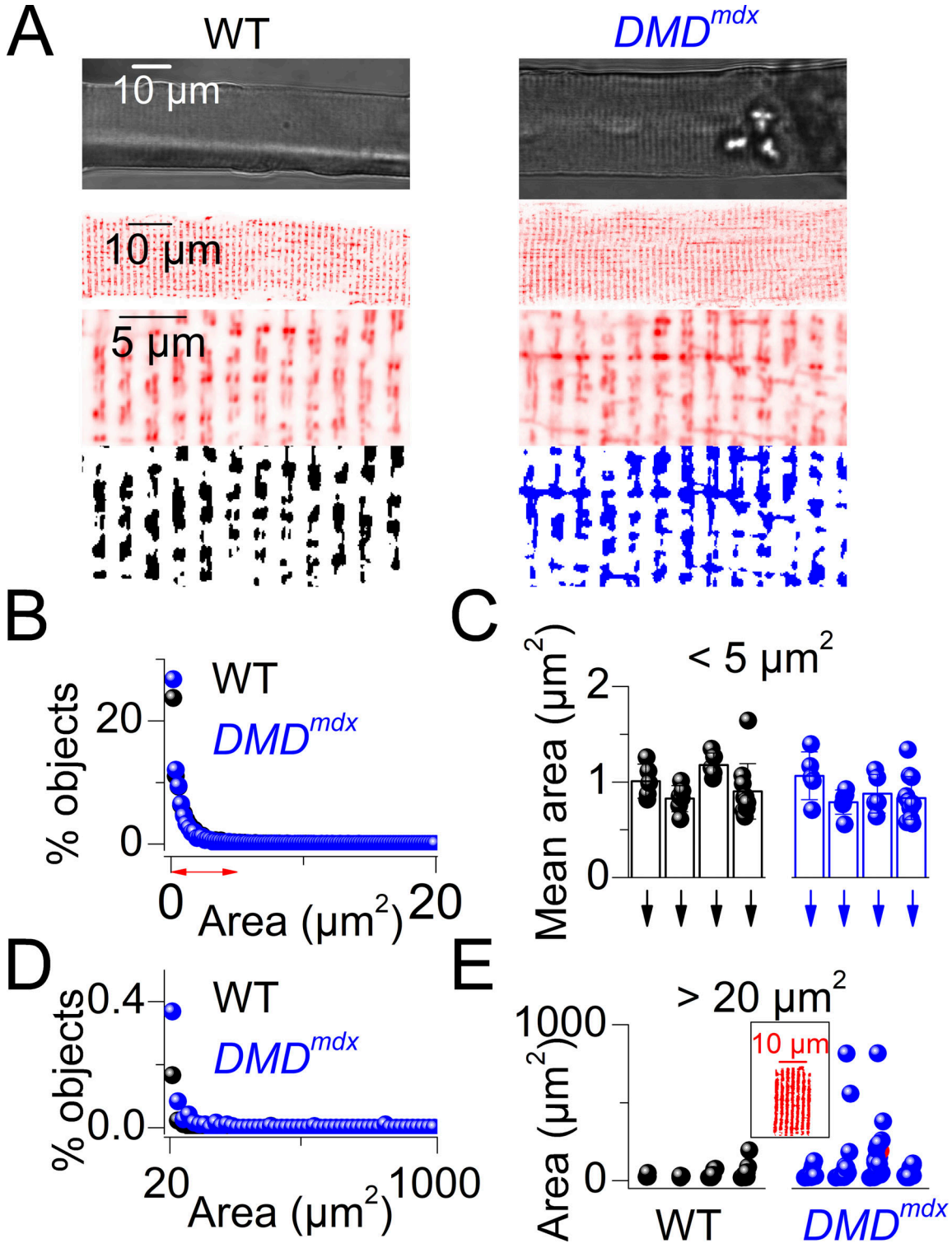

Figure 3. **TMRM staining of mitochondria in WT and *DMD*^{mdx} muscle fibers. (A)** Confocal images of TMRM fluorescence in a WT and in a *DMD*^{mdx} fiber at two distinct magnifications. Corresponding transmitted light images are shown on top. Black and white frames at the bottom correspond to the binary images obtained after thresholding the above images. **(B)** Distribution of the values for the area of separate mitochondrial objects in the two groups, up to 20 µm^2. Each symbol corresponds to the percentage of identified objects exhibiting a given surface, with an increment of 0.2 µm^2, from all WT and *DMD*^{mdx} muscle fibers. **(C)** Individual and corresponding mean (±SD) values for the area of mitochondrial objects smaller than 5 µm^2 (data are from 26 fibers from four WT animals and 28 fibers from five *DMD*^{mdx} animals. P = 0.38, nested *t* test, 95% CI for the difference between mean values: −0.29 to 0.13). Each bar and superimposed data points correspond to data from a same animal (arrows point to the series of large events detected in the same groups of fibers in E). **(D)** Distribution of the values for the area of mitochondrial objects >20 µm^2 in the two groups. Each symbol corresponds to the percentage of identified objects exhibiting a given surface, with an increment of 50 µm^2, from all WT and *DMD*^{mdx} muscle fibers. **(E)** Individual values for the area of all mitochondrial objects >20 µm^2 in fibers from each animal (each column of data points corresponds to fibers from the same animal as in C; each symbol corresponds to an individual

area in a given fiber). The red inset shows an example of binary image from a large object detected in a DMD^{mdx} fiber (190 µm², corresponding data point also shown in red in the graph). 95% CI, 95% confidence interval.

Particle analysis showed that the large majority of spatially individualized objects occupied an area <5 µm² in both groups (Fig. 3 B), likely corresponding to single pairs of mitochondria on both sides of the Z line. Mean values for the area of this class of objects did not differ between WT and DMD^{mdx} fibers (Fig. 3 C). When examining larger objects, the frequency was increased in DMD^{mdx} fibers with 117 objects larger than 20 µm² detected in a total of 21 out of 28 fibers, as compared with 38 detected in a total of 15 out of 26 WT fibers (Fig. 3, D–E). A nested *t* test comparing the number of large events (>20 µm², Fig. 3 E) detected in each tested fiber from the different animals in the two groups showed that the mean number was significantly elevated in the DMD group (P = 0.043). It should be acknowledged that since TMRM accumulation is driven by mitochondrial membrane potential, we cannot exclude a difference in the density of undetected, depolarized mitochondria between WT and DMD^{mdx} fibers. Nevertheless, we can at least ascertain that the density of polarized mitochondria is similar in the two groups.

Passive electrical properties

Dystrophin, together with its associated protein complex, is believed to play an important role in securing plasma membrane stability, to the point of preventing membrane rupturing/tearing, which are commonly admitted consequences of dystrophin deficiency. Measurements of ion current across the plasma membrane should help define whether leakiness is enhanced in the DMD muscle fibers. Using voltage clamp, we compared the properties of the membrane current at rest and in response to small hyperpolarizing pulses between WT and DMD^{mdx} fibers. The capacitance of each voltage-clamped fiber portion was estimated from the running integral of the transient current change elicited by a −20-mV pulse from −80 mV. The inset in Fig. 4 A shows the capacitive current surges at the onset and termination of the pulse, averaged from all tested WT (black) and DMD^{mdx} fibers (blue). The two bar-and-dot graphs in Fig. 4 A show individual and mean values for capacitance in fibers from each animal in the two groups. Unexpectedly, values were significantly larger in DMD^{mdx} than in WT fibers (Fig. 4 A, P = 0.006) with the overall mean value being 1.65 times that in WT fibers. Since fiber apparent width did not differ between the two groups (Fig. 1) and a similar length of fiber portion was always left outside the silicone (typically ∼150–200 µm), this suggests an elevated density of the plasma membrane in fibers from the DMD^{mdx} model. The bottom graph in Fig. 4 A shows another representation of this dataset with capacitance values plotted versus the corresponding amount of surface membrane approximated from the length and apparent width (assumed to be representative of the diameter) of each fiber, assuming it is a cylinder. Fitting a linear relationship in each group gave values consistent with commonly admitted levels of t-tubule/surface membrane ratio, but with a value 1.5 times larger in the DMD^{mdx} group. Fig. 4, B and D, shows the individual and mean absolute values for holding current (at −80 mV) and for the steady change in current elicited by the −20-mV pulse, respectively, from the same fibers. Those did not differ between the two groups. However, when normalized to the corresponding capacitance, values for both holding current (Fig. 4 C) and steady change upon −20-mV hyperpolarization (Fig. 4 E) are significantly lower in DMD^{mdx} fibers as compared with WT fibers (P = 0.005 and 0.02, respectively).

Voltage-activated $Ca_V1.1$ Ca^{2+} current

$Ca_V1.1$ is the most well accredited (Robin and Allard, 2015) and characterized Ca^{2+} entry pathway in differentiated muscle fibers. Considering the amount of literature pointing to exacerbated Ca^{2+} entry in dystrophin-deficient muscle cells, assessing $Ca_V1.1$ channel function in DMD^{mdx} fibers was of prime interest. Our measurements of the membrane current taken in response to 0.5-s-long depolarizing pulses of increasing amplitude showed that the current exhibited very similar properties in the two groups (Fig. 5 A), and none of the parameters fitted from the voltage dependency of the peak current differed between WT and DMD^{mdx} fibers (Fig. 5, B and C).

Voltage-activated SR Ca^{2+} release

Fig. 6 shows representative Ca^{2+} release datasets from a WT fiber (left) and from a DMD^{mdx} fiber (right). A line-scan F/F_0 image taken during application of a pulse to −10 mV is shown in Fig. 6 A. Fig. 6 B shows the superimposed line-averaged F/F_0 traces from the two fibers in response to all tested pulses. The corresponding calculated traces for the rate of Ca^{2+} release (Fig. 6 C) displayed the classical early peak, the amplitude of which increased with the pulse amplitude, that declined rapidly toward a very small level in both groups. For intermediate voltages, a hump-like component was routinely detected most likely reflecting the Ca^{2+} storage/release function of calsequestrin in the SR lumen (Royer et al., 2010). Overall, the time course of the fluorescence transients and of the corresponding release fluxes presented no specific feature in DMD^{mdx} fibers that would visually distinguish them from those in WT fibers. But, the maximum amplitude of the peak Ca^{2+} release was lower in the diseased condition. The running integral of each Ca^{2+} release trace during the voltage pulses is shown in Fig. 6 D. Despite a maximum peak amplitude of Ca^{2+} release smaller by ∼25% in the DMD^{mdx} fiber, the maximum amount of released Ca^{2+} (expressed with respect to the myoplasmic volume) was similar in the two fibers. All values for peak Ca^{2+} release and total amount of released Ca^{2+} from the tested 29 WT fibers and 27 DMD^{mdx} fibers are presented, versus voltage, in Fig. 7, A and B, respectively. The voltage dependency of peak Ca^{2+} release in each fiber was fitted with a Boltzmann function, the result of which is shown as a superimposed curve on each corresponding dataset in Fig. 7 A. Individual values (circles) and corresponding mean (±SD) values (from groups of fibers from the same animal, bars) for maximum peak Ca^{2+} release, mid-activation voltage, and slope factor are presented in Fig. 8, A–C, respectively, whereas values for the

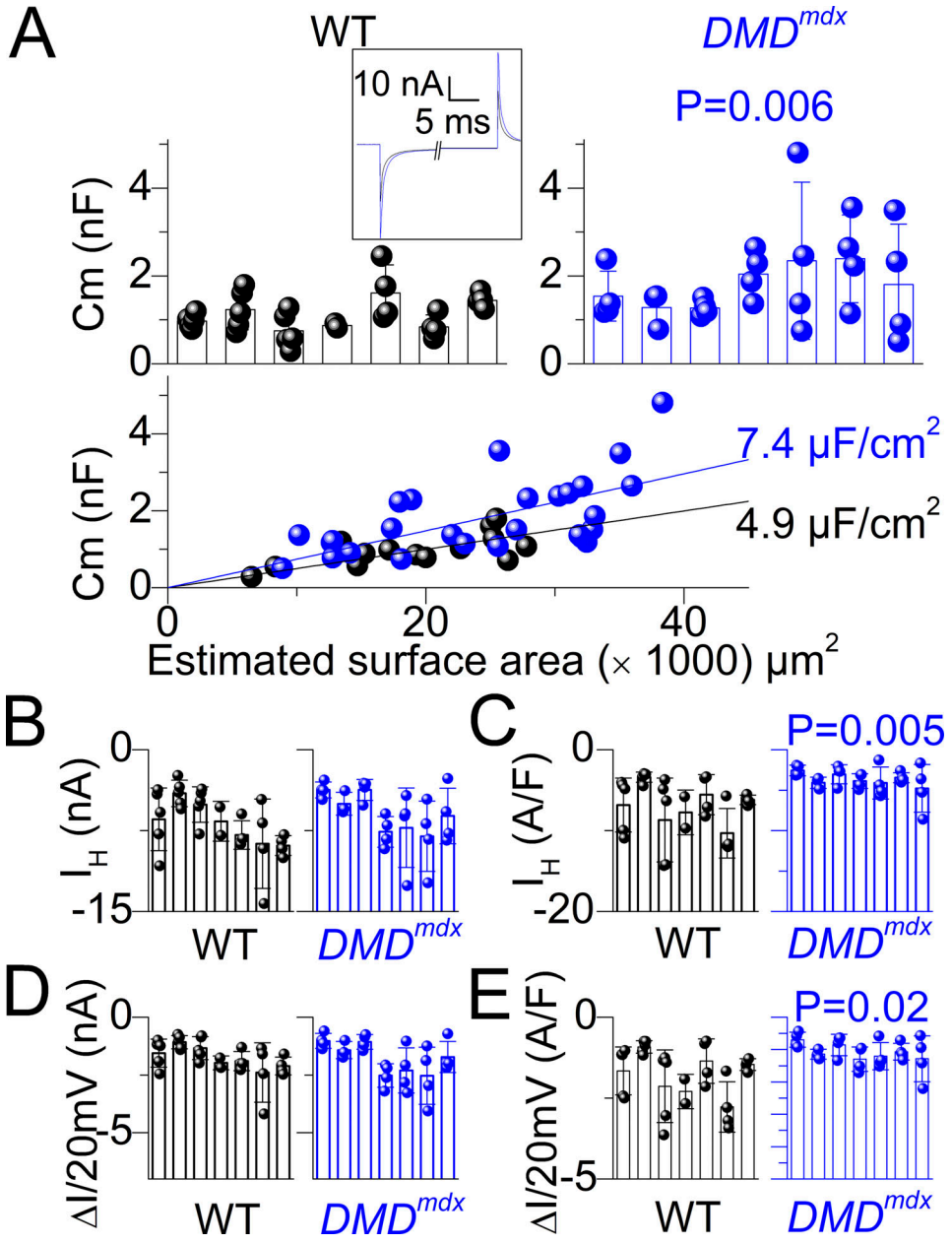

Figure 4. **Membrane current in WT and *DMD*^{mdx} muscle fibers. (A)** Individual and corresponding mean (±SD) values for the capacitance (Cm in nanofarad, nF) of WT and *DMD*^{mdx} fibers (n = 29 fibers from seven WT animals and n = 27 fibers from seven *DMD*^{mdx} animals. P = 0.006, nested t test). Each bar and superimposed data points correspond to data from a same animal. The inset shows the mean membrane current transients at the onset and termination of a −20 mV pulse from −80 mV, from all tested WT and in *DMD*^{mdx} muscle fibers. The bottom graph shows values for the capacitance as a function of the estimated surface membrane area of each corresponding fiber. Straight lines correspond to the result of a linear fit in each group. **(B)** Individual and mean (±SD) absolute values for holding current (I_H) in WT and *DMD*^{mdx} fibers (n = 29 fibers from seven WT animals and n = 27 fibers from seven *DMD*^{mdx} animals. P = 0.42, nested t test, 95% CI for the difference between mean values: −1.35 to 3.00). Each bar and superimposed data points correspond to data from a same animal. **(C)** Corresponding individual and mean (±SD) values for the holding current normalized to the capacitance (P = 0.005, nested t test). **(D)** Individual and corresponding mean (±SD) absolute values for the steady change in membrane current (ΔI/20 mV) measured at the end of the −20 mV pulse (P = 0.85, nested t test, 95% CI for the difference between mean values: −0.73 to 0.61). **(E)** Corresponding individual and mean (±SD) values for the steady current, normalized to the capacitance (P = 0.02, nested t test). 95% CI, 95% confidence interval.

total amount of released Ca^{2+} for the largest pulse (to +60 mV) are in Fig. 8 D. Statistical analysis showed that the maximum peak amplitude of Ca^{2+} release was significantly depressed in the *DMD*^{mdx} fibers by 25% as compared with WT fibers, whereas all other parameters did not differ. The preserved total amount of released Ca^{2+} in the *DMD*^{mdx} group indicates that the time course of the release flux must differ from that in the WT group. To test for this, in each fiber, the decay of Ca^{2+} release triggered by the pulse to +60 mV was fitted with a two-exponential plus constant function. Values for the parameters (amplitude and time constant for the fast and slow components, and final level/constant) were compared using the nested analysis. Respective values in

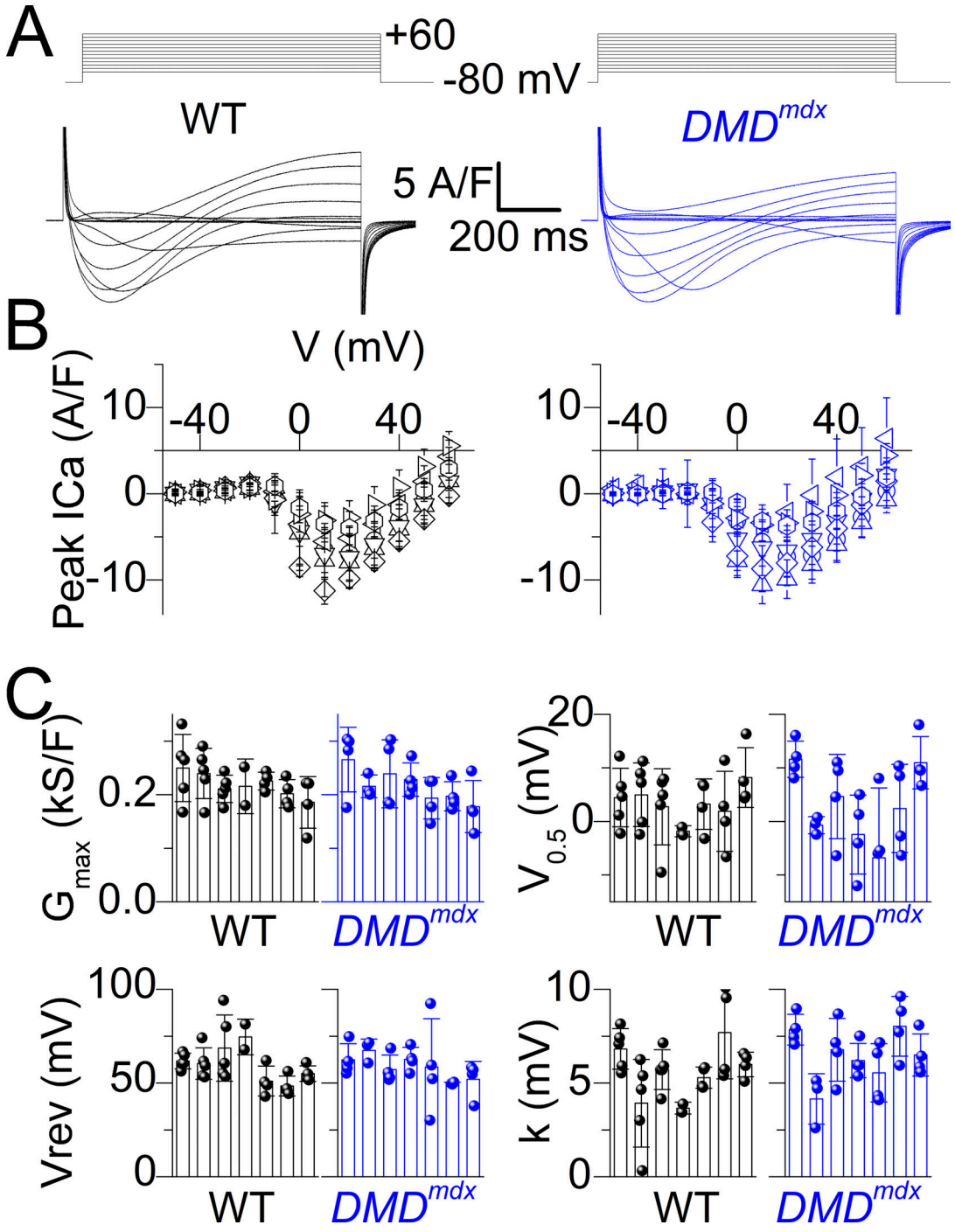

Figure 5. **Voltage-activated $Ca_V1.1$ Ca^{2+} current in WT and *DMD*^{mdx} muscle fibers. (A)** Representative examples of Ca^{2+} current traces in the two groups, in response to the indicated pulse protocol. **(B)** Values for the peak Ca^{2+} current versus voltage in WT and *DMD*^{mdx} fibers (data are from 29 fibers from seven WT animals and 27 fibers from seven *DMD*^{mdx} animals). For the sake of clarity, only mean (±SD) values from fibers from a same animal are shown. **(C)** Individual and corresponding mean (±SD) values for the parameters (G_{max} the maximum conductance, $V_{0.5}$ the mid-voltage, V_{rev} the reversal potential, and k the slope factor) fitted from the peak current versus voltage relationship in each fiber. Each bar and superimposed data points correspond to data from a same animal. For G_{max}, $V_{0.5}$, V_{rev}, and k, P = 0.85, 0.79, 0.79, and 0.29, respectively (nested *t* tests, corresponding 95% CIs for the difference between mean values: −0.035 to 0.029, −6.83 to 5.32, −9.58 to 7.46, and −0.77 to 2.39, respectively). 95% CI, 95% confidence interval.

WT (n = 7) and *DMD*^{mdx} animals (n = 7) for the amplitude (mean of 36.6 ± 10.3 versus 32.2 ± 3.8 $\mu M.ms^{-1}$) and time constant (mean of 4.3 ± 1.2 versus 6.0 ± 1.9 ms) of the fast component and for the final level (mean of 0.34 ± 0.18 versus 0.34 ± 0.17 $\mu M.ms^{-1}$) did not differ. In contrast, the slow exponential component in the *DMD*^{mdx} group exhibited a reduced amplitude (mean of 26.7 ± 6.7 versus 49.1 ± 14.8 $\mu M.ms^{-1}$, P = 0.002) and a larger time constant (mean of 53.7 ± 14.9 versus 30.2 ± 9.6 ms, P = 0.007). Thus, the slower late decay of Ca^{2+} release in the *DMD*^{mdx} fibers may well explain for the lack of significant

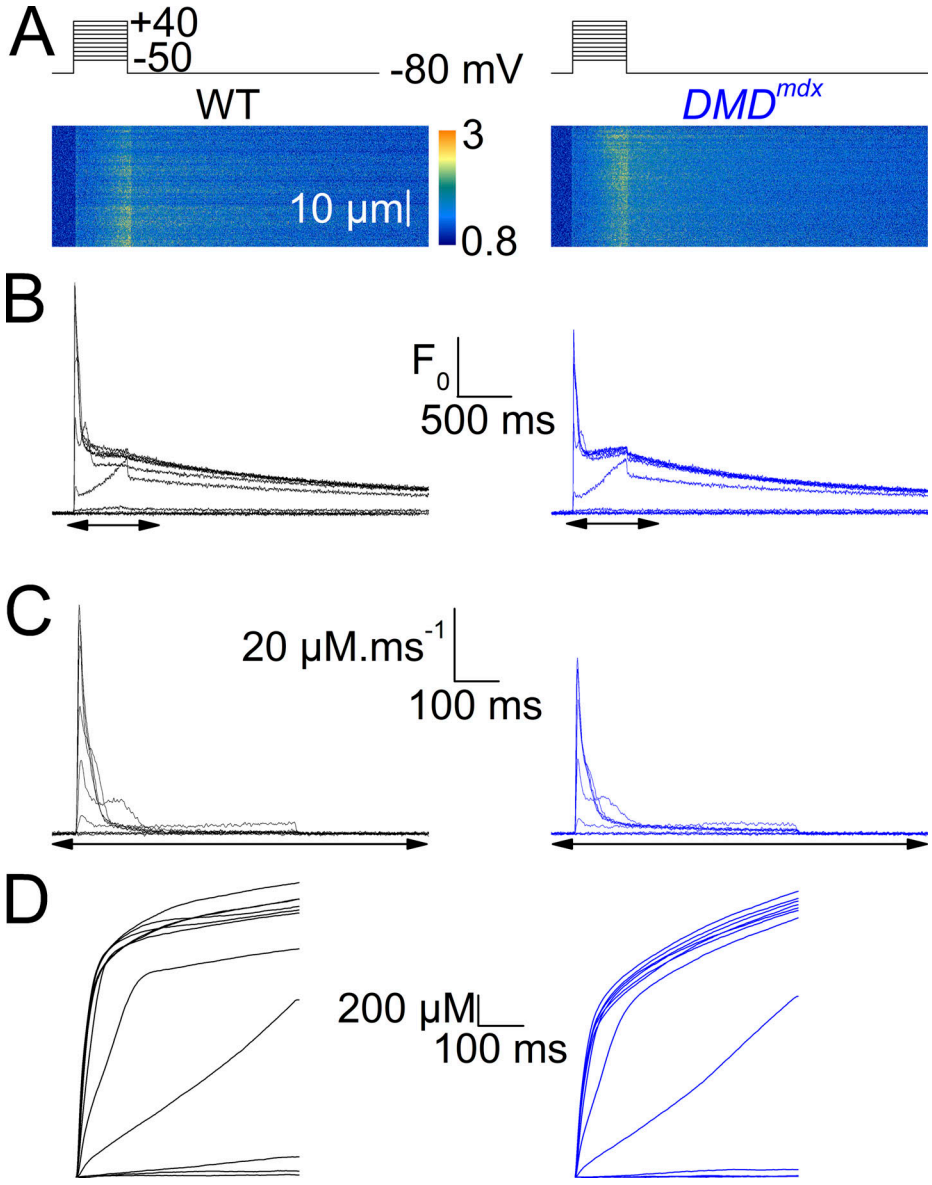

Figure 6. **Voltage-activated SR Ca^{2+} release in WT and *DMD*^{mdx} muscle fibers. (A)** Examples of confocal line-scan images of rhod-2 fluorescence collected from a WT and from a *DMD*^{mdx} muscle fiber, while applying a depolarizing pulse to −10 mV. **(B)** Line-averaged rhod-2 fluorescence changes elicited by the pulses shown on top, in the same WT and *DMD*^{mdx} fibers as in A. **(C)** Rate of SR Ca^{2+} release calculated from the rhod-2 F/F_0 records shown in B. **(D)** Running integral of the SR Ca^{2+} flux traces shown in C during the depolarizing pulses.

difference in total Ca^{2+} released between the two groups, despite the lower peak amplitude in the *DMD*^{mdx} group.

Spontaneous Ca^{2+} release at rest

Enhanced SR Ca^{2+} leak through RYR1 channels was proposed to contribute to dysfunction and damage of dystrophic muscle fibers (Bellinger et al., 2009). Because we have previously revealed RYR1 overactivity at rest, in the form of Ca^{2+} sparks, in intact muscle fibers from other models of muscle diseases (Kutchukian et al., 2017, 2019), we tested whether this would be also the case in the *DMD*^{mdx} condition. The bottom images in Fig. 9 A correspond to the SD of Fluo-4 fluorescence intensity at each pixel position, along a sequence of 40 consecutive *x,y* confocal frames. Local spots of elevated SD correspond to locations of Ca^{2+} sparks occurrence. In these conditions, a few sparks were routinely detected, in both the WT and the *DMD*^{mdx} fibers. The relative fiber area showing sparks activity was quantified. Individual values from each fiber and corresponding mean values from fibers from a same animal are shown in Fig. 9 B. Values were very low: <0.5% of the fiber's area presented with Ca^{2+} release activity, consistent with the notorious very low incidence or absence, of Ca^{2+} sparks in healthy intact mammalian muscle fibers. There was no significant difference between the WT and the *DMD*^{mdx} groups.

APs

Lack of dystrophin in muscle cells is presumed to impair plasma membrane stability so that contraction would induce membrane

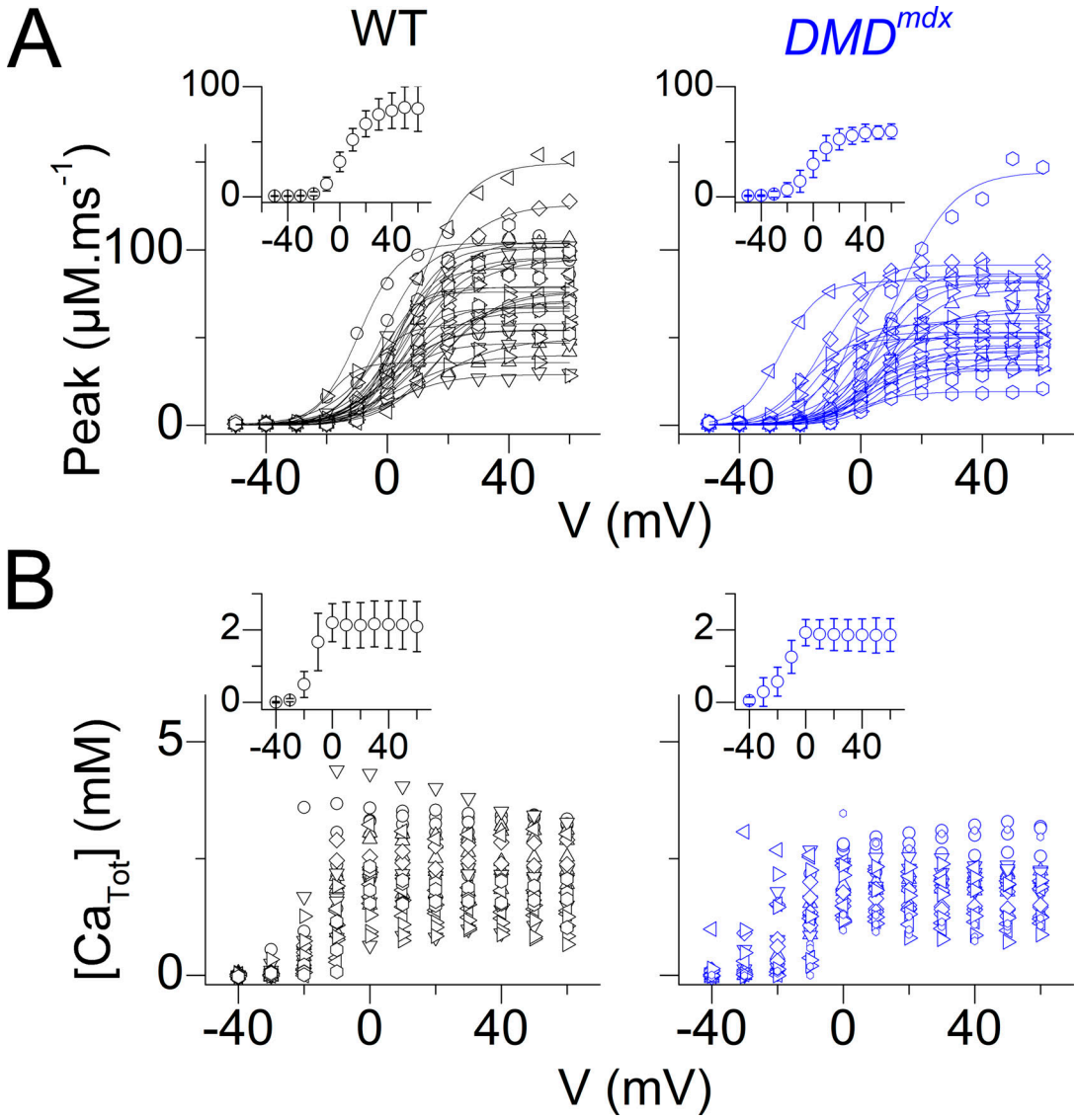

Figure 7. **Voltage dependence of SR Ca^{2+} release in WT and *DMD*^{mdx} muscle fibers. (A)** Values for peak SR Ca^{2+} release flux versus voltage in all tested WT and *DMD*^{mdx} muscle fibers (data are from 29 fibers from seven WT animals and 27 fibers from seven *DMD*^{mdx} animals). An identical symbol is used for fibers from a same animal. Each dataset was fitted with a Boltzmann function (superimposed lines). The inset in each graph shows the mean (±SD) values calculated using the average from fibers from a same animal (n = 7 in each group). **(B)** Corresponding values for the voltage dependency of the total amount of released Ca^{2+} in the two groups of fibers.

rupture and/or impairment of excitability; this would be involved in muscle strength loss (Petrof et al., 1993; Call et al., 2013; Roy et al., 2016). With the aim of identifying functional signs of such processes, we challenged WT and *DMD*^{mdx} muscle fibers with trains of APs, in the absence of intracellular Ca^{2+} buffering, thus allowing full contraction of the fiber portion under study. Representative examples of trains of APs are shown in Fig. 10, from a WT and a *DMD*^{mdx} muscle fiber at the different tested frequencies. Overall, we found no indication that electrical activity of the diseased fibers would be specifically sensitive to either repeated or tetanic contractions. Fig. 11 presents values for the voltage level preceding each AP and for the peak amplitude of each AP, during the course of the trains, at the different frequencies, in each fiber tested. At 80 Hz, two out of six WT fibers and four out of eight *DMD*^{mdx} fibers presented with a substantial drop in AP amplitude. Otherwise, in no case did we detect depolarization of the resting (pre-AP) levels that would witness substantial membrane damage and or loss of excitability. We also quantified the rate of voltage return to the resting level, at the end of the 20, 50, and 80 Hz trains, by fitting an exponential function to this time course (highlighted in red in Fig. 10): there was no significant difference between the groups of WT and *DMD*^{mdx} fibers. With respect to single AP properties, peak values did not differ between the two groups but the half-width was significantly enhanced (P = 0.02) in the *DMD*^{mdx} condition with mean (±SD) values of 1.45 ± 0.27 (n = 4 fibers), 1.46 ± 0.1 (n = 3), and 1.24 ± 0.13 ms (n = 3) in the fibers from three WT animals, and 1.61 ± 0.19 (n = 4), 1.76 ± 0.34 (n = 4), and 1.60 ± 0.09 ms (n = 3), in fibers from three *DMD*^{mdx} animals.

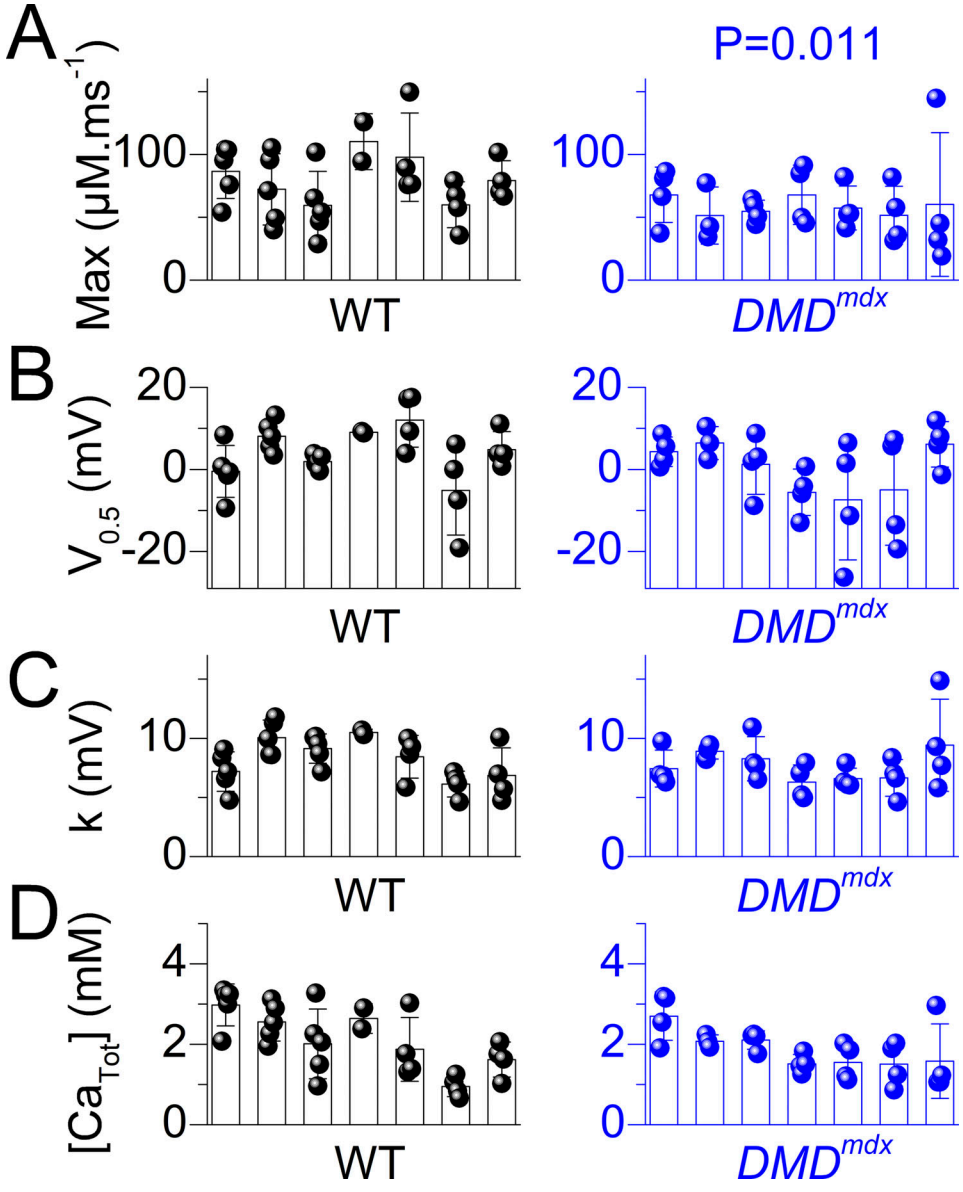

Figure 8. **SR Ca^{2+} release parameters in WT and *DMD*^{mdx} muscle fibers. (A–D)** Individual and corresponding mean (±SD) values for maximum rate of SR Ca^{2+} release (Max), voltage of mid-activation ($V_{0.5}$), slope factor (k), and total amount of released Ca^{2+} ($[Ca_{Tot}]$), respectively, in WT and *DMD*^{mdx} fibers (data are from 29 fibers from seven WT animals and 27 fibers from seven *DMD*^{mdx} animals). Each bar and superimposed data points correspond to data from a same animal. Values in A–C were obtained from fitting a Boltzmann function to the peak SR Ca^{2+} release versus voltage relationships. For Max, $V_{0.5}$, k, and $[Ca_{Tot}]$, P = 0.011, 0.21, 0.42, and 0.49, respectively (nested *t* test). For $V_{0.5}$, k, and $[Ca_{Tot}]$, the 95% CIs for the difference between mean values are: −11.07 to 2.69, −2.29 to 1.03, and −910.6 to 461.5, respectively. 95% CI, 95% confidence interval.

Discussion

Multiple molecular and cellular consequences of dystrophin deficiency have been documented (see for instance Allen et al. [2016]), but the exact mechanisms that determine muscle fibers weakness and muscle fibers necrosis in DMD remain controversial. Altered Ca^{2+} fluxes affecting intracellular Ca^{2+} handling has been proposed, for >40 years (e.g., Bodensteiner and Engel, 1978), to underlie or at least contribute. However, despite recurrent authoritative statements in the literature regarding the critical role of Ca^{2+} entry across the plasma membrane or of Ca^{2+} leak across the SR membrane, direct evidence of how exactly (and quantitatively to what extent and along which time frame) these mechanisms affect muscle fiber function and integrity remains nebulous. Further understanding of these issues requires detailed knowledge of the functional properties of the diseased muscle fibers, keeping in mind that conditions allowing either control or reading of the plasma membrane voltage are precious when it comes to investigate the properties of transmembrane Ca^{2+} fluxes and of SR Ca^{2+} release. We used here a combination of electrophysiology and imaging that has proved efficient in the past to identify and quantify defects in Ca^{2+} signaling and EC coupling in other muscle diseases (e.g., Kutchukian et al., 2016, 2017, 2019; Huntoon et al., 2018; Pelletier et al., 2020; Silva-Rojas et al., 2022). We applied this

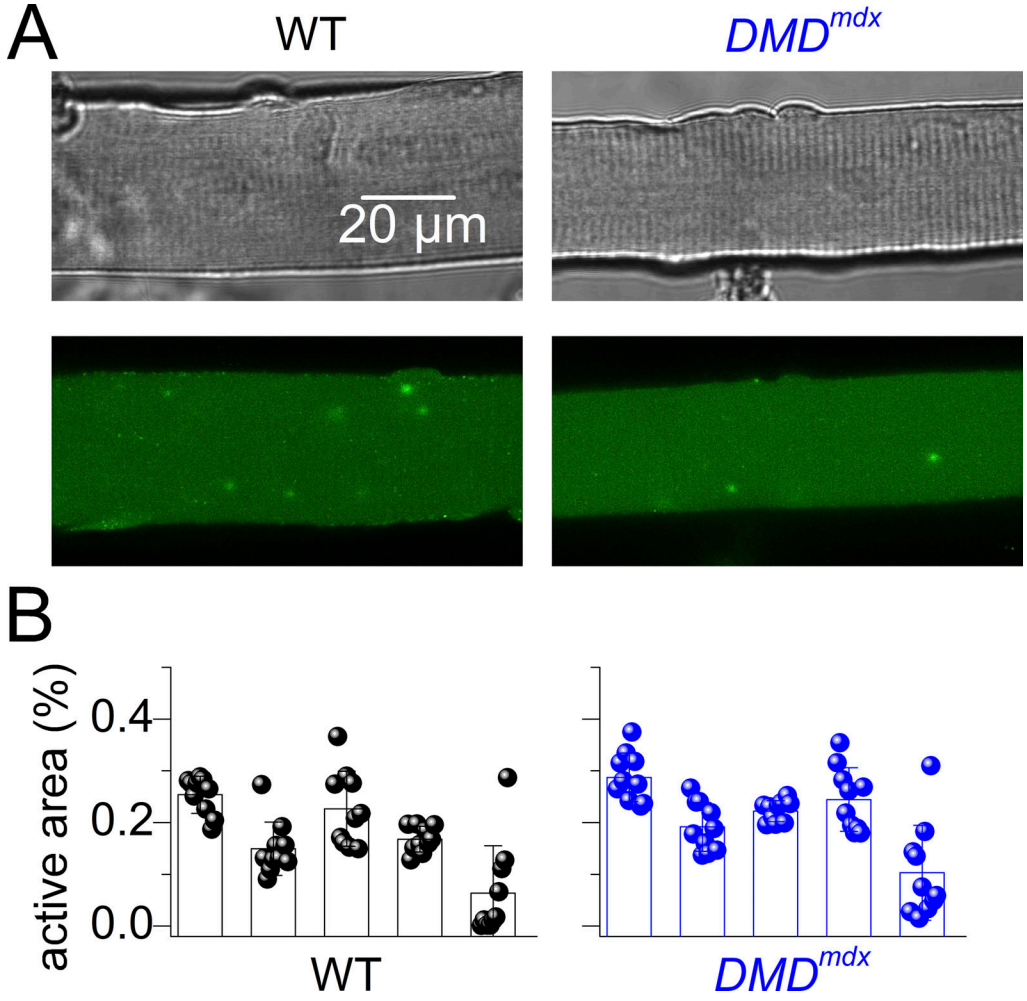

Figure 9. **SR Ca^{2+} release events at rest in WT and DMD^{mdx} muscle fibers. (A)** Green images show the spatial distribution of the SD of Fluo-4 fluorescence intensity throughout a sequence of 40 *x,y* consecutive confocal frames, in a WT and in a DMD^{mdx} muscle fiber. Transmitted light images of the two fibers are shown on top. **(B)** Individual and corresponding mean (±SD) values for the relative fiber area exhibiting spontaneous Ca^{2+} release in the two groups (data are from 50 fibers from five animals in each group. P = 0.42, nested *t* test, 95% CI for the difference between mean values: −0.065 to 0.14). Each bar and superimposed data points correspond to data from a same animal. 95% CI, 95% confidence interval.

combination to muscle fibers isolated from a rat model (DMD^{mdx}) that reproduces the DMD patient's condition better than the standard *mdx* mouse. One limitation of the preparation is that collagenase treatment was used for isolation, so that the extracellular matrix is largely removed. Intact isolated DMD^{mdx} muscle fibers looked fine, with no sign of widespread or local sarcomere shortening (Fig. 2 B) that would be expected in the presence of membrane damage. Measurements of the apparent width of the FDB muscle fibers showed no difference between the WT and DMD^{mdx} groups, which contrasts with the smaller diameter values reported by Larcher et al. (2014) in DMD^{mdx} fibers, from analysis of frozen sections from the biceps femoris muscles. It cannot be excluded that the FDB muscles exhibit a milder phenotype than the biceps femoris muscles. However, diameter values determined from a muscle section cannot distinguish between non-branched and branched fibers, and it is very possible that this contributed to the difference between the two studies, as we did not consider branched fibers in our analysis. Membrane current measurements also provided no indication for an increase in the resting membrane conductance that would also be anticipated from a leaky or damaged plasma membrane. WT and DMD^{mdx} fibers contracting in response to trains of APs behaved very similarly, with no sign that the contractile activity would specifically affect plasma membrane polarization in the diseased fibers. Of course, one cannot exclude that more stringent conditions, for instance eccentric contractions (Call et al., 2013), are required to induce membrane damage and/or electrophysiological alterations in the diseased fibers. However, single muscle fiber measurements of either the membrane current or membrane voltage are very sensitive to the integrity of the plasma membrane and, with respect to the widely acknowledged concepts of membrane frailty and rupturing, that are traditionally associated with dystrophin deficiency, we find it puzzling that this does not show in the electrical measurements.

In fully differentiated fibers, t-tubules and mitochondria form dense, well-organized networks. The t-tubule network integrity is mandatory for proper EC coupling function. Our di-

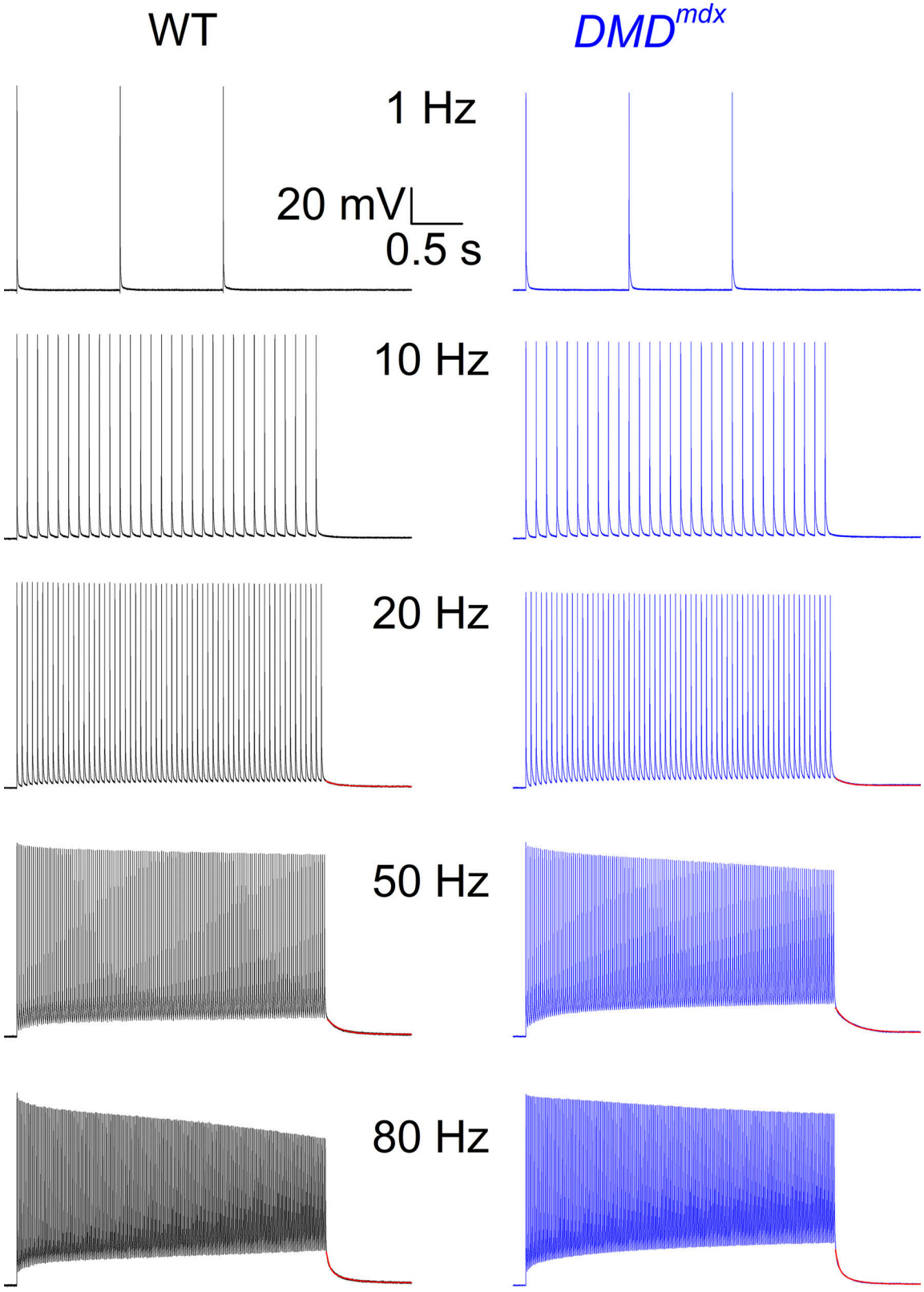

Figure 10. **Trains of APs in WT and *DMD*^{mdx} muscle fibers.** Representative records of the changes in membrane voltage elicited by short suprathreshold depolarizing current pulses delivered during 3 s at the indicated frequency, in a WT and in a *DMD*^{mdx} muscle fiber. Superimposed red lines at the end of the 20-, 50-, and 80-Hz records correspond to the result of a single exponential fit (see text for details, section: APs).

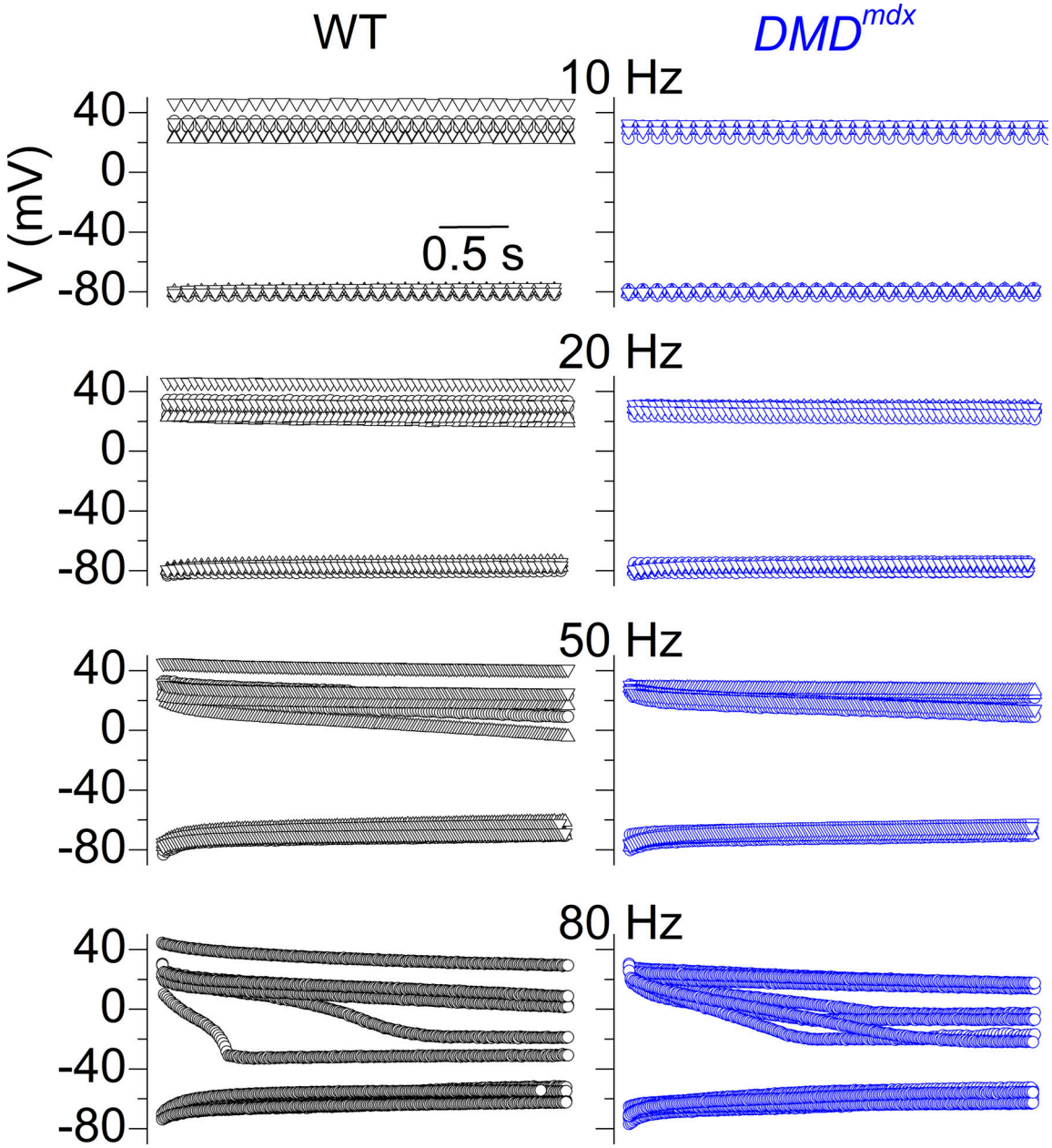

Figure 11. **Evolution of the membrane voltage during the course of 3-s-long trains of APs.** Graphs show voltage values measured just before each AP and at the peak value in all tested WT and *DMD*^{mdx} muscle fibers (data are from 10 fibers from three WT animals and 11 fibers from three *DMD*^{mdx} animals). An identical symbol is used for fibers from a same animal.

8-anepps images did not show any obvious alteration in the *DMD*^{mdx} fibers, at least nothing that would come any close to the t-tubule loss observed, for instance, in muscle fibers from the mouse model of myotubular myopathy (Al Qusairi et al., 2009; Kutchukian et al., 2016), which make fibers suffer from EC coupling failure (Szentesi et al., 2023). On the contrary and quite intriguing, we found that *DMD*^{mdx} fibers presented with a larger capacitance than WT fibers. This may result from enhanced t-tubule tortuosity at a resolution level inaccessible to di-8-anepps imaging. Interesting in this respect are results from early electron microscopy studies of biopsies from DMD patients, which described alterations of the t-tubule system taking the form of abnormal course and tangle formation (Oguchi and Tsukagoshi, 1980; Oguchi et al., 1982). We are currently exploring the possibility that this is happening in the *DMD*^{mdx} muscle fibers.

With respect to mitochondria, there have been reports of changes in mitochondria morphology and of concurrent metabolic defects in dystrophic muscle, possibly related to altered mitochondrial Ca^{2+} content (Pant et al., 2015; Moore et al., 2020; see Mareedu et al., 2021), although absence of differences in aspects of mitochondrial content and dynamics has also been reported (Barker et al., 2018). Our TMRM measurements showed that the global mitochondrial network pattern is similar

in WT and *DMD*^{mdx} fibers, with a majority of small single objects in the two populations. Interesting though was the propensity for more numerous large objects (area >20 µm^2) in *DMD*^{mdx} fibers that, we speculate, may be related to the previously acknowledged changes in mitochondria dynamics and mitophagy in dystrophin-deficient muscle cells (Pant et al., 2015; Reid and Alexander, 2021).

Properties of the $Ca_V1.1$ Ca^{2+} current are unaffected in *DMD*^{mdx} fibers. Although this Ca^{2+} entry is not mandatory for muscle function (Dayal et al., 2017), our data at least prove that there is no enhanced Ca^{2+} entry through $Ca_V1.1$ in the *DMD*^{mdx} fibers, which does not exclude that it may occur through alternate pathways. This result may also be viewed with reference to muscle disease conditions affecting EC coupling, with depressed SR Ca^{2+} release being paralleled by depressed $Ca_V1.1$ Ca^{2+} current (Al Qusairi et al., 2009; Kutchukian et al., 2017; Huntoon et al., 2018; Pelletier et al., 2020; Silva-Rojas et al., 2022). The situation is obviously different here, even though the maximum peak amplitude of Ca^{2+} release was depressed by a similar extent as, for instance, in the model of myopathy due to reduction in RYR1 content (Pelletier et al., 2020). This indicates that the reason for reduced Ca^{2+} release in *DMD*^{mdx} fibers is likely to be mechanistically distinct. In comparison, previous studies using the *mdx* mouse provided contrasting results, some groups reporting reduced SR Ca^{2+} release in the *mdx* fibers (Woods et al., 2004; Hollingworth et al., 2008), whereas other reported either minor or no differences with the WT fibers (Head, 1993; Collet et al., 1999; Tutdibi et al., 1999). Here, the reduced peak SR Ca^{2+} release occurred with no significant change in the total amount of released Ca^{2+} at the end of the 0.5-s-long pulses. A lower SR content, which could occur as a consequence of an increased SR Ca^{2+} leak, was thus likely not involved. Also arguing against an enhanced SR Ca^{2+} leak in the *DMD*^{mdx} fibers was the absence of any difference in the spontaneous Ca^{2+} release activity at rest.

Altogether, the present characterization of intact *DMD*^{mdx} muscle fibers failed to identify functional signs of plasma membrane compromised integrity, fragility, unspecific leakiness, or enhanced Ca^{2+} entry across $Ca_V1.1$ channels. It though revealed a significant reduction of peak SR Ca^{2+} release during EC coupling, the extent of which (25%) likely contributes to muscle weakness, without being expected to dramatically compromise muscle function (if remaining at that level). We found no indication that this decrease is related to an enhanced SR Ca^{2+} leakage. We cannot exclude that the previously proposed enhanced plasma and SR membrane leakiness to Ca^{2+} occur within a range and/or time scale that are not accessible to our measurements. We also cannot exclude that the pathophysiological impact of such alterations is of limited relevance with respect to the dramatic outcome of the disease in terms of muscle function and integrity.

In summary, muscle fibers from 3-mo-old *DMD*^{mdx} rats present no obvious deleterious alteration of plasma/t-tubule membrane properties that would be consistent with fragility, compromised excitability, or excess Ca^{2+} entry. Yet, these fibers exhibit a reduced maximum rate of voltage-activated SR Ca^{2+} release, which likely contributes to depressed force production, without being expected to dramatically impair muscle function. Future investigations at later stages of the disease should help define whether these features remain stable or deteriorate as the disease progresses.

Data availability

All generated datasets are presented in the article. Raw data will be made available upon reasonable request to the corresponding author.

Acknowledgments

Eduardo Ríos served as editor.

This work was supported by grants from the Centre National de la Recherche Scientifique, the Institut national de la santé et de la recherche médicale, and Université Claude Bernard - Lyon 1 to Institut NeuroMyoGène—Pathophysiology and Genetics of Neuron and Muscle (CNRS UMR5261- INSERM U1315). This work was also supported by the Association Française contre les Myopathies (AFM-Téléthon: Alliance MyoNeurALP2 program, project # 4.1.1 to V. Jacquemond).

Author contributions: J. Schreiber: formal analysis, investigation, and writing—review and editing. L. Rotard: formal analysis, investigation, visualization, and writing—review and editing. Y. Tourneur: formal analysis and software. A. Lafoux: resources. C. Berthier: project administration and supervision. B. Allard: conceptualization and writing—review and editing. C. Huchet: methodology, resources, validation, and writing—review and editing. V. Jacquemond: conceptualization, data curation, formal analysis, funding acquisition, investigation, methodology, project administration, resources, supervision, validation, visualization, and writing—original draft, review, and editing.

Disclosures: The authors declare no competing interests exist.

Submitted: 9 April 2024
Revised: 14 August 2024
Revised: 20 November 2024
Accepted: 6 December 2024

References

Al-Qusairi, L., N. Weiss, A. Toussaint, C. Berbey, N. Messaddeq, C. Kretz, D. Sanoudou, A.H. Beggs, B. Allard, J.L. Mandel, et al. 2009. T-tubule disorganization and defective excitation-contraction coupling in muscle fibers lacking myotubularin lipid phosphatase. *Proc. Natl. Acad. Sci. USA*. 106:18763–18768. https://doi.org/10.1073/pnas.0900705106

Allen, D.G., N.P. Whitehead, and S.C. Froehner. 2016. Absence of dystrophin disrupts skeletal muscle signaling: Roles of Ca2+, reactive oxygen species, and nitric oxide in the development of muscular dystrophy. *Physiol. Rev.* 96:253–305. https://doi.org/10.1152/physrev.00007.2015

Balghi, H., S. Sebille, B. Constantin, S. Patri, V. Thoreau, L. Mondin, E. Mok, A. Kitzis, G. Raymond, and C. Cognard. 2006a. Mini-dystrophin expression down-regulates overactivation of G protein-mediated IP3 signaling pathway in dystrophin-deficient muscle cells. *J. Gen. Physiol.* 127:171–182. https://doi.org/10.1085/jgp.200509456

Balghi, H., S. Sebille, L. Mondin, A. Cantereau, B. Constantin, G. Raymond, and C. Cognard. 2006b. Mini-dystrophin expression down-regulates IP3-mediated calcium release events in resting dystrophin-deficient muscle cells. *J. Gen. Physiol.* 128:219–230. https://doi.org/10.1085/jgp.200609559

Barker, R.G., V.L. Wyckelsma, H. Xu, and R.M. Murphy. 2018. Mitochondrial content is preserved throughout disease progression in the mdx mouse

model of Duchenne muscular dystrophy, regardless of taurine supplementation. *Am. J. Physiol. Cell Physiol.* 314:C483–C491. https://doi.org/10.1152/ajpcell.00046.2017

Bellinger, A.M., S. Reiken, C. Carlson, M. Mongillo, X. Liu, L. Rothman, S. Matecki, A. Lacampagne, and A.R. Marks. 2009. Hypernitrosylated ryanodine receptor calcium release channels are leaky in dystrophic muscle. *Nat. Med.* 15:325–330. https://doi.org/10.1038/nm.1916

Bellissimo, C.A., M.C. Garibotti, and C.G.R. Perry. 2022. Mitochondrial stress responses in Duchenne muscular dystrophy: Metabolic dysfunction or adaptive reprogramming? *Am. J. Physiol. Cell Physiol.* 323:C718–C730. https://doi.org/10.1152/ajpcell.00249.2022

Bodensteiner, J.B., and A.G. Engel. 1978. Intracellular calcium accumulation in Duchenne dystrophy and other myopathies: A study of 567,000 muscle fibers in 114 biopsies. *Neurology*. 28:439–446. https://doi.org/10.1212/WNL.28.5.439

Boittin, F.X., O. Petermann, C. Hirn, P. Mittaud, O.M. Dorchies, E. Roulet, and U.T. Ruegg. 2006. Ca2+-independent phospholipase A2 enhances store-operated Ca2+ entry in dystrophic skeletal muscle fibers. *J. Cell Sci.* 119:3733–3742. https://doi.org/10.1242/jcs.03184

Call, J.A., G.L. Warren, M. Verma, and D.A. Lowe. 2013. Acute failure of action potential conduction in mdx muscle reveals new mechanism of contraction-induced force loss. *J. Physiol.* 591:3765–3776. https://doi.org/10.1113/jphysiol.2013.254656

Cárdenas, C., N. Juretić, J.A. Bevilacqua, I.E. García, R. Figueroa, R. Hartley, A.L. Taratuto, R. Gejman, N. Riveros, J. Molgó, and E. Jaimovich. 2010. Abnormal distribution of inositol 1,4,5-trisphosphate receptors in human muscle can be related to altered calcium signals and gene expression in Duchenne dystrophy-derived cells. *FASEB J.* 24:3210–3221. https://doi.org/10.1096/fj.09-152017

Cea, L.A., C. Puebla, B.A. Cisterna, R. Escamilla, A.A. Vargas, M. Frank, P. Martínez-Montero, C. Prior, J. Molano, I. Esteban-Rodríguez, et al. 2016. Fast skeletal myofibers of mdx mouse, model of Duchenne muscular dystrophy, express connexin hemichannels that lead to apoptosis. *Cell. Mol. Life Sci.* 73:2583–2599. https://doi.org/10.1007/s00018-016-2132-2

Chamberlain, J.S., J. Metzger, M. Reyes, D. Townsend, and J.A. Faulkner. 2007. Dystrophin-deficient mdx mice display a reduced life span and are susceptible to spontaneous rhabdomyosarcoma. *FASEB J.* 21:2195–2204. https://doi.org/10.1096/fj.06-7353com

Cheng, H., W.J. Lederer, and M.B. Cannell. 1993. Calcium sparks: Elementary events underlying excitation-contraction coupling in heart muscle. *Science*. 262:740–744. https://doi.org/10.1126/science.8235594

Collet, C., B. Allard, Y. Tourneur, and V. Jacquemond. 1999. Intracellular calcium signals measured with indo-1 in isolated skeletal muscle fibres from control and mdx mice. *J. Physiol.* 520:417–429. https://doi.org/10.1111/j.1469-7793.1999.00417.x

Cully, T.R., J.N. Edwards, O. Friedrich, D.G. Stephenson, R.M. Murphy, and B.S. Launikonis. 2012. Changes in plasma membrane Ca-ATPase and stromal interacting molecule 1 expression levels for Ca(2+) signaling in dystrophic mdx mouse muscle. *Am. J. Physiol. Cell Physiol.* 303:C567–C576. https://doi.org/10.1152/ajpcell.00144.2012

Cully, T.R., and B.S. Launikonis. 2016. Leaky ryanodine receptors delay the activation of store overload-induced Ca2+ release, a mechanism underlying malignant hyperthermia-like events in dystrophic muscle. *Am. J. Physiol. Cell Physiol.* 310:C673–C680. https://doi.org/10.1152/ajpcell.00366.2015

Cully, T.R., and G.G. Rodney. 2020. Nox4 - RyR1 - Nox2: Regulators of microdomain signaling in skeletal muscle. *Redox Biol.* 36:101557. https://doi.org/10.1016/j.redox.2020.101557

Dayal, A., K. Schrötter, Y. Pan, K. Föhr, W. Melzer, and M. Grabner. 2017. The Ca^{2+} influx through the mammalian skeletal muscle dihydropyridine receptor is irrelevant for muscle performance. *Nat. Commun.* 8:475. https://doi.org/10.1038/s41467-017-00629-x

Desai, S., S. Grefte, E. van de Westerlo, S. Lauwen, A. Paters, J.H.M. Prehn, Z. Gan, J. Keijer, M.J.W. Adjobo-Hermans, and W.J.H. Koopman. 2023. Performance of TMRM and Mitotrackers in mitochondrial morpho-functional analysis of primary human skin fibroblasts. *Biochim. Biophys. Acta Bioenerg.* 1865:149027. https://doi.org/10.1016/j.bbabio.2023.149027

Divet, A., and C. Huchet-Cadiou. 2002. Sarcoplasmic reticulum function in slow- and fast-twitch skeletal muscles from mdx mice. *Pflugers Arch.* 444:634–643. https://doi.org/10.1007/s00424-002-0854-5

Doran, P., P. Dowling, J. Lohan, K. McDonnell, S. Poetsch, and K. Ohlendieck. 2004. Subproteomics analysis of Ca+-binding proteins demonstrates decreased calsequestrin expression in dystrophic mouse skeletal muscle. *Eur. J. Biochem.* 271:3943–3952. https://doi.org/10.1111/j.1432-1033.2004.04332.x

Ducret, T., C. Vandebrouck, M.L. Cao, J. Lebacq, and P. Gailly. 2006. Functional role of store-operated and stretch-activated channels in murine adult skeletal muscle fibres. *J. Physiol.* 575:913–924. https://doi.org/10.1113/jphysiol.2006.115154

Edwards, J.N., O. Friedrich, T.R. Cully, F. von Wegner, R.M. Murphy, and B.S. Launikonis. 2010. Upregulation of store-operated Ca2+ entry in dystrophic mdx mouse muscle. *Am. J. Physiol. Cell Physiol.* 299:C42–C50. https://doi.org/10.1152/ajpcell.00524.2009

Eisner, D.A. 2021. Pseudoreplication in physiology: More means less. *J. Gen. Physiol.* 153:e202012826. https://doi.org/10.1085/jgp.202012826

Fong, P.Y., P.R. Turner, W.F. Denetclaw, and R.A. Steinhardt. 1990. Increased activity of calcium leak channels in myotubes of Duchenne human and mdx mouse origin. *Science*. 250:673–676. https://doi.org/10.1126/science.2173137

Franco, A. Jr., and J.B. Lansman. 1990. Calcium entry through stretch-inactivated ion channels in mdx myotubes. *Nature*. 344:670–673. https://doi.org/10.1038/344670a0

Garcia, J., and M.F. Schneider. 1993. Calcium transients and calcium release in rat fast-twitch skeletal muscle fibres. *J. Physiol.* 463:709–728. https://doi.org/10.1113/jphysiol.1993.sp019618

García-Castañeda, M., A. Michelucci, N. Zhao, S. Malik, and R.T. Dirksen. 2022. Postdevelopmental knockout of Orai1 improves muscle pathology in a mouse model of Duchenne muscular dystrophy. *J. Gen. Physiol.* 154:e202213081. https://doi.org/10.1085/jgp.202213081

Gervásio, O.L., N.P. Whitehead, E.W. Yeung, W.D. Phillips, and D.G. Allen. 2008. TRPC1 binds to caveolin-3 and is regulated by Src kinase - role in Duchenne muscular dystrophy. *J. Cell Sci.* 121:2246–2255. https://doi.org/10.1242/jcs.032003

Ghasemizadeh, A., E. Christin, A. Guiraud, N. Couturier, M. Abitbol, V. Risson, E. Girard, C. Jagla, C. Soler, L. Laddada, et al. 2021. MACF1 controls skeletal muscle function through the microtubule-dependent localization of extra-synaptic myonuclei and mitochondria biogenesis. *Elife*. 10:e70490. https://doi.org/10.7554/eLife.70490

Head, S.I. 1993. Membrane potential, resting calcium and calcium transients in isolated muscle fibres from normal and dystrophic mice. *J. Physiol.* 469:11–19. https://doi.org/10.1113/jphysiol.1993.sp019801

Hollingworth, S., U. Zeiger, and S.M. Baylor. 2008. Comparison of the myoplasmic calcium transient elicited by an action potential in intact fibres of mdx and normal mice. *J. Physiol.* 586:5063–5075. https://doi.org/10.1113/jphysiol.2008.160507

Huntoon, V., J.J. Widrick, C. Sanchez, S.M. Rosen, C. Kutchukian, S. Cao, C.R. Pierson, X. Liu, M.A. Perrella, A.H. Beggs, et al. 2018. SPEG-deficient skeletal muscles exhibit abnormal triad and defective calcium handling. *Hum. Mol. Genet.* 27:1608–1617. https://doi.org/10.1093/hmg/ddy068

Jaque-Fernandez, F., A. Beaulant, C. Berthier, L. Monteiro, B. Allard, M. Casas, J. Rieusset, and V. Jacquemond. 2020. Preserved Ca^{2+} handling and excitation-contraction coupling in muscle fibres from diet-induced obese mice. *Diabetologia*. 63:2471–2481. https://doi.org/10.1007/s00125-020-05256-8

Jaque-Fernandez, F., B. Allard, L. Monteiro, A. Lafoux, C. Huchet, E. Jaimovich, C. Berthier, and V. Jacquemond. 2023. Probenecid affects muscle Ca2+ homeostasis and contraction independently from pannexin channel block. *J. Gen. Physiol.* 155:e202213203. https://doi.org/10.1085/jgp.202213203

Jiang, T., D. Yeung, C.F. Lien, and D.C. Górecki. 2005. Localized expression of specific P2X receptors in dystrophin-deficient DMD and mdx muscle. *Neuromuscul. Disord.* 15:225–236. https://doi.org/10.1016/j.nmd.2004.11.008

Kargacin, M.E., and G.J. Kargacin. 1996. The sarcoplasmic reticulum calcium pump is functionally altered in dystrophic muscle. *Biochim. Biophys. Acta*. 1290:4–8. https://doi.org/10.1016/0304-4165(95)00180-8

Krüger, J., C. Kunert-Keil, F. Bisping, and H. Brinkmeier. 2008. Transient receptor potential cation channels in normal and dystrophic mdx muscle. *Neuromuscul. Disord.* 18:501–513. https://doi.org/10.1016/j.nmd.2008.04.003

Kutchukian, C., M. Lo Scrudato, Y. Tourneur, K. Poulard, A. Vignaud, C. Berthier, B. Allard, M.W. Lawlor, A. Buj-Bello, and V. Jacquemond. 2016. Phosphatidylinositol 3-kinase inhibition restores Ca $^{2+}$ release defects and prolongs survival in myotubularin-deficient mice. *Proc. Natl. Acad. Sci. USA*. 113:14432–14437. https://doi.org/10.1073/pnas.1604099113

Kutchukian, C., P. Szentesi, B. Allard, D. Trochet, M. Beuvin, C. Berthier, Y. Tourneur, P. Guicheney, L. Csernoch, M. Bitoun, and V. Jacquemond. 2017. Impaired excitation-contraction coupling in muscle fibres from the dynamin2^{R465W} mouse model of centronuclear myopathy. *J. Physiol.* 595:7369–7382. https://doi.org/10.1113/JP274990

Kutchukian, C., P. Szentesi, B. Allard, A. Buj-Bello, L. Csernoch, and V. Jacquemond. 2019. Ca2+-induced sarcoplasmic reticulum Ca2+ release in myotubularin-deficient muscle fibers. *Cell Calcium*. 80:91–100. https://doi.org/10.1016/j.ceca.2019.04.004

Larcher, T., A. Lafoux, L. Tesson, S. Remy, V. Thepenier, V. François, C. Le Guiner, H. Goubin, M. Dutilleul, L. Guigand, et al. 2014. Characterization of dystrophin deficient rats: A new model for duchenne muscular dystrophy. *PLoS One*. 9:e110371. https://doi.org/10.1371/journal.pone.0110371

Lin, B.L., J.Y. Shin, W.P. Jeffreys, N. Wang, C.A. Lukban, M.C. Moorer, E. Velarde, O.A. Hanselman, S. Kwon, S. Kannan, et al. 2022. Pharmacological TRPC6 inhibition improves survival and muscle function in mice with Duchenne muscular dystrophy. *JCI Insight*. 7:e158906. https://doi.org/10.1172/jci.insight.158906

Lohan, J., and K. Ohlendieck. 2004. Drastic reduction in the luminal Ca2+-binding proteins calsequestrin and sarcalumenin in dystrophin-deficient cardiac muscle. *Biochim. Biophys. Acta*. 1689:252–258. https://doi.org/10.1016/j.bbadis.2004.04.002

Mallouk, N., and B. Allard. 2002. Ca(2+) influx and opening of Ca(2+)-activated K(+) channels in muscle fibers from control and mdx mice. *Biophys. J.* 82:3012–3021. https://doi.org/10.1016/S0006-3495(02)75642-7

Mareedu, S., E.D. Million, D. Duan, and G.J. Babu. 2021. Abnormal calcium handling in duchenne muscular dystrophy: Mechanisms and potential therapies. *Front. Physiol.* 12:647010. https://doi.org/10.3389/fphys.2021.647010

Matsumura, C.Y., A.P. Taniguti, A. Pertille, H. Santo Neto, and M.J. Marques. 2011. Stretch-activated calcium channel protein TRPC1 is correlated with the different degrees of the dystrophic phenotype in mdx mice. *Am. J. Physiol. Cell Physiol.* 301:C1344–C1350. https://doi.org/10.1152/ajpcell.00056.2011

McGreevy, J.W., C.H. Hakim, M.A. McIntosh, and D. Duan. 2015. Animal models of duchenne muscular dystrophy: From basic mechanisms to gene therapy. *Dis. Model. Mech.* 8:195–213. https://doi.org/10.1242/dmm.018424

Millay, D.P., S.A. Goonasekera, M.A. Sargent, M. Maillet, B.J. Aronow, and J.D. Molkentin. 2009. Calcium influx is sufficient to induce muscular dystrophy through a TRPC-dependent mechanism. *Proc. Natl. Acad. Sci. USA*. 106:19023–19028. https://doi.org/10.1073/pnas.0906591106

Mondin, L., H. Balghi, B. Constantin, C. Cognard, and S. Sebille. 2009. Negative modulation of inositol 1,4,5-trisphosphate type 1 receptor expression prevents dystrophin-deficient muscle cells death. *Am. J. Physiol. Cell Physiol.* 297:C1133–C1145. https://doi.org/10.1152/ajpcell.00048.2009

Mokri, B., and A.G. Engel. 1975. Duchenne dystrophy: Electron microscopic findings pointing to a basic or early abnormality in the plasma membrane of the muscle fiber. *Neurology*. 25:1111–1120. https://doi.org/10.1212/WNL.25.12.1111

Moore, T.M., A.J. Lin, A.R. Strumwasser, K. Cory, K. Whitney, T. Ho, T. Ho, J.L. Lee, D.H. Rucker, C.Q. Nguyen, et al. 2020. Mitochondrial dysfunction is an early consequence of partial or complete dystrophin loss in mdx mice. *Front. Physiol.* 11:690. https://doi.org/10.3389/fphys.2020.00690

Morine, K.J., M.M. Sleeper, E.R. Barton, and H.L. Sweeney. 2010. Overexpression of SERCA1a in the mdx diaphragm reduces susceptibility to contraction-induced damage. *Hum. Gene Ther.* 21:1735–1739. https://doi.org/10.1089/hum.2010.077

Nakamura, K., W. Fujii, M. Tsuboi, J. Tanihata, N. Teramoto, S. Takeuchi, K. Naito, K. Yamanouchi, and M. Nishihara. 2014. Generation of muscular dystrophy model rats with a CRISPR/Cas system. *Sci. Rep.* 4:5635. https://doi.org/10.1038/srep05635

Niebroj-Dobosz, I., S. Kornguth, H. Schutta, F.L. Siegel, and I. Hausmanowa-Petrusewicz. 1989a. Proteins of muscle subcellular fractions in Duchenne progressive muscular dystrophy stained with "stains-all" cationic carbocyanine dye and with Coomassie Blue. *Muscle Nerve*. 12:273–280. https://doi.org/10.1002/mus.880120404

Niebroj-Dobosz, I., S. Kornguth, H.S. Schutta, and F.L. Siegel. 1989b. Elevated calmodulin levels and reduced calmodulin-stimulated calcium-ATPase in Duchenne progressive muscular dystrophy. *Neurology*. 39:1610–1614. https://doi.org/10.1212/WNL.39.12.1610

Nouet, J., E. Himelman, K.C. Lahey, Q. Zhao, and D. Fraidenraich. 2020. Connexin-43 reduction prevents muscle defects in a mouse model of manifesting Duchenne muscular dystrophy female carriers. *Sci. Rep.* 10:5683. https://doi.org/10.1038/s41598-020-62844-9

Oguchi, K., and H. Tsukagoshi. 1980. An electron-microscopic study of the T-system in progressive muscular dystrophy (Duchenne) using lanthanum. *J. Neurol. Sci.* 44:161–168. https://doi.org/10.1016/0022-510X(80)90124-0

Oguchi, K., N. Yanagisawa, and H. Tsukagoshi. 1982. The structure of the T-system in human muscular dystrophy. A high-voltage electron-microscopic study. *J. Neurol. Sci.* 57:333–341. https://doi.org/10.1016/0022-510X(82)90039-9

Pant, M., D.H. Sopariwala, N.C. Bal, J. Lowe, D.A. Delfín, J. Rafael-Fortney, and M. Periasamy. 2015. Metabolic dysfunction and altered mitochondrial dynamics in the utrophin-dystrophin deficient mouse model of duchenne muscular dystrophy. *PLoS One*. 10:e0123875. https://doi.org/10.1371/journal.pone.0123875

Pasternak, C., S. Wong, and E.L. Elson. 1995. Mechanical function of dystrophin in muscle cells. *J. Cell Biol.* 128:355–361. https://doi.org/10.1083/jcb.128.3.355

Pastoret, C., and A. Sebille. 1995. Mdx mice show progressive weakness and muscle deterioration with age. *J. Neurol. Sci.* 129:97–105. https://doi.org/10.1016/0022-510X(94)00276-T

Pelletier, L., A. Petiot, J. Brocard, B. Giannesini, D. Giovannini, C. Sanchez, L. Travard, M. Chivet, M. Beaufils, C. Kutchukian, et al. 2020. In vivo RyR1 reduction in muscle triggers a core-like myopathy. *Acta Neuropathol. Commun.* 8:192. https://doi.org/10.1186/s40478-020-01068-4

Pertille, A., C.L. de Carvalho, C.Y. Matsumura, H.S. Neto, and M.J. Marques. 2010. Calcium-binding proteins in skeletal muscles of the mdx mice: Potential role in the pathogenesis of duchenne muscular dystrophy. *Int. J. Exp. Pathol.* 91:63–71. https://doi.org/10.1111/j.1365-2613.2009.00688.x

Pestronk, A., I.M. Parhad, D.B. Drachman, and D.L. Price. 1982. Membrane myopathy: Morphological similarities to Duchenne muscular dystrophy. *Muscle Nerve*. 5:209–214. https://doi.org/10.1002/mus.880050306

Petrof, B.J., J.B. Shrager, H.H. Stedman, A.M. Kelly, and H.L. Sweeney. 1993. Dystrophin protects the sarcolemma from stresses developed during muscle contraction. *Proc. Natl. Acad. Sci. USA*. 90:3710–3714. https://doi.org/10.1073/pnas.90.8.3710

Quinlan, J.G., H.S. Hahn, B.L. Wong, J.N. Lorenz, A.S. Wenisch, and L.S. Levin. 2004. Evolution of the mdx mouse cardiomyopathy: Physiological and morphological findings. *Neuromuscul. Disord.* 14:491–496. https://doi.org/10.1016/j.nmd.2004.04.007

Reid, A.L., and M.S. Alexander. 2021. The interplay of mitophagy and inflammation in duchenne muscular dystrophy. *Life*. 11:648. https://doi.org/10.3390/life11070648

Robin, G., and B. Allard. 2015. Voltage-gated Ca(2+) influx through L-type channels contributes to sarcoplasmic reticulum Ca(2+) loading in skeletal muscle. *J. Physiol.* 593:4781–4797. https://doi.org/10.1113/JP270252

Roy, P., F. Rau, J. Ochala, J. Messéant, B. Fraysse, J. Lainé, O. Agbulut, G. Butler-Browne, D. Furling and A. Ferry. 2016. Dystrophin restoration therapy improves both the reduced excitability and the force drop induced by lengthening contractions in dystrophic mdx skeletal muscle. *Skelet. Muscle*. 6:23. https://doi.org/10.1186/s13395-016-0096-4

Royer, L., M. Sztretye, C. Manno, S. Pouvreau, J. Zhou, B.C. Knollmann, F. Protasi, P.D. Allen, and E. Ríos. 2010. Paradoxical buffering of calcium by calsequestrin demonstrated for the calcium store of skeletal muscle. *J. Gen. Physiol.* 136:325–338. https://doi.org/10.1085/jgp.201010454

Sanchez, C., C. Berthier, Y. Tourneur, L. Monteiro, B. Allard, L. Csernoch, and V. Jacquemond. 2021. Detection of Ca2+ transients near ryanodine receptors by targeting fluorescent Ca2+ sensors to the triad. *J. Gen. Physiol.* 153:e202012592. https://doi.org/10.1085/jgp.202012592

Schneider, J.S., M. Shanmugam, J.P. Gonzalez, H. Lopez, R. Gordan, D. Fraidenraich, and G.J. Babu. 2013. Increased sarcolipin expression and decreased sarco(endo)plasmic reticulum Ca2+ uptake in skeletal muscles of mouse models of Duchenne muscular dystrophy. *J. Muscle Res. Cell Motil.* 34:349–356. https://doi.org/10.1007/s10974-013-9350-0

Schuhmeier, R.P., and W. Melzer. 2004. Voltage-dependent Ca2+ fluxes in skeletal myotubes determined using a removal model analysis. *J. Gen. Physiol.* 123:33–51. https://doi.org/10.1085/jgp.200308908

Silva-Rojas, R., V. Nattarayan, F. Jaque-Fernandez, R. Gomez-Oca, A. Menuet, D. Reiss, M. Goret, N. Messaddeq, V.M. Lionello, C. Kretz, et al. 2022. Mice with muscle-specific deletion of Bin1 recapitulate centronuclear myopathy and acute downregulation of dynamin 2 improves their phenotypes. *Mol. Ther.* 30:868–880. https://doi.org/10.1016/j.ymthe.2021.08.006

Sikkel, M.B., D.P. Francis, J. Howard, F. Gordon, C. Rowlands, N.S. Peters, A.R. Lyon, S.E. Harding, and K.T. MacLeod. 2017. Hierarchical statistical techniques are necessary to draw reliable conclusions from analysis of isolated cardiomyocyte studies. *Cardiovasc. Res.* 113:1743–1752. https://doi.org/10.1093/cvr/cvx151

Stedman, H.H., H.L. Sweeney, J.B. Shrager, H.C. Maguire, R.A. Panettieri, B. Petrof, M. Narusawa, J.M. Leferovich, J.T. Sladky, and A.M. Kelly. 1991. The mdx mouse diaphragm reproduces the degenerative changes of Duchenne muscular dystrophy. *Nature*. 352:536–539. https://doi.org/10.1038/352536a0

Stuckey, D.J., C.A. Carr, P. Camelliti, D.J. Tyler, K.E. Davies, and K. Clarke. 2012. In vivo MRI characterization of progressive cardiac dysfunction in the mdx mouse model of muscular dystrophy. *PLoS One*. 7:e28569. https://doi.org/10.1371/journal.pone.0028569

Szentesi, P., B. Dienes, C. Kutchukian, T. Czirjak, A. Buj-Bello, V. Jacquemond, and L. Csernoch. 2023. Disrupted T-tubular network accounts for asynchronous calcium release in MTM1-deficient skeletal muscle. *J. Physiol.* 601:99–121. https://doi.org/10.1113/JP283650

Taglietti, V., K. Kefi, I. Bronisz-Budzyńska, B. Mirciloglu, M. Rodrigues, N. Cardone, F. Coulpier, B. Periou, C. Gentil, M. Goddard, et al. 2022. Duchenne muscular dystrophy trajectory in R-DMDdel52 preclinical rat model identifies COMP as biomarker of fibrosis. *Acta Neuropathol. Commun.* 10:60. https://doi.org/10.1186/s40478-022-01355-2

Teichmann, M.D., F.V. Wegner, R.H. Fink, J.S. Chamberlain, B.S. Launikonis, B. Martinac, and O. Friedrich. 2008. Inhibitory control over Ca(2+) sparks via mechanosensitive channels is disrupted in dystrophin deficient muscle but restored by mini-dystrophin expression. *PLoS One*. 3: e3644. https://doi.org/10.1371/journal.pone.0003644

Tanabe, Y., K. Esaki, and T. Nomura. 1986. Skeletal muscle pathology in X chromosome-linked muscular dystrophy (mdx) mouse. *Acta Neuropathol.* 69:91–95. https://doi.org/10.1007/BF00687043

Tutdibi, O., H. Brinkmeier, R. Rüdel, and K.J. Föhr. 1999. Increased calcium entry into dystrophin-deficient muscle fibres of MDX and ADR-MDX mice is reduced by ion channel blockers. *J. Physiol.* 515:859–868. https://doi.org/10.1111/j.1469-7793.1999.859ab.x

Van Erp, C., D. Loch, N. Laws, A. Trebbin, and A.J. Hoey. 2010. Timeline of cardiac dystrophy in 3-18-month-old MDX mice. *Muscle Nerve*. 42: 504–513. https://doi.org/10.1002/mus.21716

Vandebrouck, C., D. Martin, M. Colson-Van Schoor, H. Debaix, and P. Gailly. 2002. Involvement of TRPC in the abnormal calcium influx observed in dystrophic (mdx) mouse skeletal muscle fibers. *J. Cell Biol.* 158: 1089–1096. https://doi.org/10.1083/jcb.200203091

Willmann, R., S. Possekel, J. Dubach-Powell, T. Meier, and M.A. Ruegg. 2009. Mammalian animal models for Duchenne muscular dystrophy. *Neuromuscul. Disord.* 19:241–249. https://doi.org/10.1016/j.nmd.2008.11.015

Wilson, K., C. Faelan, J.C. Patterson-Kane, D.G. Rudmann, S.A. Moore, D. Frank, J. Charleston, J. Tinsley, G.D. Young, and A.J. Milici. 2017. Duchenne and becker muscular dystrophies: A review of animal models, clinical end points, and biomarker quantification. *Toxicol. Pathol.* 45: 961–976. https://doi.org/10.1177/0192623317734823

Woods, C.E., D. Novo, M. DiFranco, and J.L. Vergara. 2004. The action potential-evoked sarcoplasmic reticulum calcium release is impaired in mdx mouse muscle fibres. *J. Physiol.* 557:59–75. https://doi.org/10.1113/jphysiol.2004.061291

Yeung, D., K. Zablocki, C.F. Lien, T. Jiang, S. Arkle, W. Brutkowski, J. Brown, H. Lochmuller, J. Simon, E.A. Barnard, and D.C. Górecki. 2006. Increased susceptibility to ATP via alteration of P2X receptor function in dystrophic mdx mouse muscle cells. *FASEB J.* 20:610–620. https://doi.org/10.1096/fj.05-4022com

Zhao, X., J.G. Moloughney, S. Zhang, S. Komazaki, and N. Weisleder. 2012. Orai1 mediates exacerbated Ca(2+) entry in dystrophic skeletal muscle. *PLoS One*. 7:e49862. https://doi.org/10.1371/journal.pone.0049862